OPEN ACCESS

Mathematical Physics

Edited by Aleksandar Sedmak
and Dragoslav Kuzmanović
University of Belgrade

Volume II - Numerical Methods

Contributors:
Aleksandar Sedmak
Simon Sedmak
Nikola Mladenović
Rade Vignjević
Sreten Mastilović

Publishing House
ESIS - PH

Mathematical Physics

Numerical Methods

A. Sedmak, S. Sedmak, N. Mladenović,
R. Vignjević, S. Mastilović

ISBN: 9788831482561

ESIS

HTTPS://WWW.STRUCTURALINTEGRITY.EU

First edition, November 2022

Contents

Preface

This book is mainly based on the material initially published in Serbian, in 2021, by the University of Belgrade, Faculty of Mining and Geology, under the title Mathematical Physics (Theory and Examples). For the purpose of this book the material from the Serbian edition was reviewed, amended, and translated, with new material added in two final chapters in the second volume. We have divided text into two separate volumes:

Mathematics of Physics - Analytical Methods and
Mathematics of Physics - Numerical Methods.

The first volume consists of 8 chapters:

- The first 7 chapters were written by Dragoslav Kuzmanović, Dobrica Nikolić and Ivan Obradović, and correspond to the text from Chapters 1-8 of the Serbian edition, translated by Ivan Obradović.
- The material of Chapter 8, which is of a monographic character, corresponds to the material of Chapter 9 in the Serbian edition, but was thoroughly reviewed and rewritten in English by Mihailo Lazarević.

The second volume consists of 6 chapters:

- The first 3 chapters were written by Aleksandar Sedmak and correspond to Chapter 10 of the Serbian edition, restructured and reviewed, and then translated by Simon Sedmak.

- Chapter 4 corresponds to the text of Chapter 11 of the Serbian edition, written and translated by Nikola Mladenović.
- Chapters 5 and 6, written by Rade Vignjević and Sreten Mastilović, respectively, offer completely new material.

Chapters 4,5 and 6 are of a monographic character.

IV Numerical method - CMD

6. Introduction to Computational Mechanics of Discontinua

6.1 Introduction

The rapid development of computational mechanics of discontinua (CMD) emerged from the need to model objectively the deformation, damage and fracture of quasi-brittle materials with random, heterogeneous (or discontinuous) micro-/meso-structure and inferior (or non-existent) tensile strength. For decades, prior to that, many researchers have tried to model these material systems using classical methods of continuum mechanics but with limited success. One of the main reasons for this "elusiveness" is that behavior of the subject materials is essentially defined by their heterogeneous/discrete character, which affects the **localization of deformation** and damage evolution through the processes of nucleation, propagation and coalescence of cracks on various sub-macroscopic spatial scales. These phenomena are inextricably linked to the discontinuity of displacement, which clearly violates the continuum hypothesis and the fundamental assumptions of differential calculus. These difficulties have led to development of CMD whose basics are briefly summarized in this introduction. Over the past few decades, CMD models have fought for their place among the tools in the structural analysis and design. Finally, nowadays, they have become complementary to continuum mechanics models and experimental methods thanks to their ability to improve our understanding of damage and fracture and the ways they affect the effective material properties.

After introductory considerations, a summary of the basic concepts of traditional methods of CMD is presented. It should be noted that this classification of methods is somewhat subjective since their boundaries are blurred, domains overlap and distinctions are iffy. Be it as it may, the tentative classification is as follows: molecular dynamics (MD) and its coarser-scale offshoot dubbed herein particle dynamics (PD), the lattice methods and the discrete element methods (DEM). Although these (particle-based) methods are now widely used to model different classes of materials and various physical phenomena and industrial processes, the most natural applications seem to be the simulations of deformation and flow, damage, and fracture of systems that have the same topology as the representative model structure. Therefore, the modern, advanced applications advocate a modeling approach where it is insisted upon, as far as possible, the direct correspondence between the experimentally determined material and the structure explicitly represented by the numerical model.

All materials have a discontinuous (and heterogeneous) structure on some spatial scale (if not macroscopic, perhaps mesoscopic, microscopic, by definition atomic) as illustrated by Figure 6.1. When this scale is "very small" from the standpoint of engineering applications, the materials are considered continuous (and homogeneous) (Figure 6.2). This discontinuity and heterogeneity lead to complex mechanical behavior difficult to reproduce with models based on the classical theory of continuum mechanics since the material substance: (i) does not fill entirely the space it occupies, and (ii) the physical and mechanical properties may vary significantly within that space and across various directions. Among these complex phenomena notable is the evolution of damage with nucleation, propagation, branching, mutual interaction and coalescence of (micro-/meso-/macro-scale) cracks and other pre-existing flaws and features of material texture that can lead to appearance of flow, diffuse or localized deformation and damage, fracture, and fragmentation. All CMD methods described herein have in common that they cope with these complexities by establishing a computational domain (approximating the material structure) by a collection of discrete building units that are, or may be, interconnected. These models differ from the computational models of continuum mechanics in the definition of the displacement field only in the finite number of nodal points and, accordingly, in the formulation of the problem using algebraic, instead of partial differential, equations.

During the 1960s, researchers and engineers working in various fields of mechanics of materials and materials science noticed that solutions obtained using traditional continuum mechanics often exhibited singularities or yielded results inconsistent with experimental observations. In the decade that followed, the awesome development of computer capabilities and the accompanying advances of numerical methods enabled the emergence of novel particle-based computational methods that used various distinct structural-building elements (atoms, springs, trusses, beams, particles or various shapes) to model materials. CMD is nowadays firmly established as an integral part of not only the cutting-edge research in various fields (e.g., nanotechnology, stem cell research, biomedical engineering, space propulsion) but also industrial processes covering a wide range of different application fields (e.g., mining, machining, pharmaceuticals, civil construction, industrial and systems engineering).

Figure 6.1: Examples of discontinuous and heterogeneous material systems with representative spatial scales. (a) epoxy-cemented glass bead material (courtesy of Idar Larsen (SINTEF) and Prof. Rune M. Holt (NTNU)), (b) ultralight metalic microlattice (on Dandelion, courtesy of Dr. Tobias A. Schaedler), (c) Gypsum sand (photgraphed by Prof. Mark A. Wilson), (d) concrete, (e) soil, (f) asphalt, (g) particle composite (Kerrock® 9057 – aluminum hydroxide particles with acrylic binder), (h) rock (Travertine /top/ and Nero Marinace Granite /bottom/), (i) rock masiffs (courtesy of Prof. Radojica Lapcevic). (Note: black/white rectangles indicate length scales.)

Modeling using computer simulations is more flexible than analytical modeling and has the advantage over experimental research in that the data are available at every stage of the virtual experiment. This flexibility extends to the ability to configure loads, initial and boundary conditions, and to tailor the custom-made models in accordance with the topological, geometric, and structural disorder of material.

These, so called, virtual experiments are in main aspects very similar to the laboratory experiments. First, a sample is prepared from the subject material rendering a simulation object in virtual space ("numerical" or "virtual" material). The sample created in this way is then connected to the necessary "virtual" measuring instruments so that the parameters of the state can be recorded over a period of time. Since most measurements are subject to statistical variations, the more time is available to average the results, the more accurate the measurements become.

However, the virtual measurement resolution is inversely proportional to the size of the averaging period and it is necessary to find a compromise between these conflicting requirements taking into account the nature of the physical phenomenon being simulated. Consequently, the most common errors made during virtual experiments are very similar to those that can contaminate the results of actual laboratory experiments: the sample is not adequately prepared; the measurement is too short; due to conceptual oversights, we do not measure what we intend to measure...

All CMD methods offer some common advantages in damage and fracture analysis compared to corresponding conventional computational methods based on continuum mechanics (typically, FEM). Damage and its evolution are presented explicitly through broken bonds or contacts; it is not necessary to use any empirical relations to define damage or determine its effect on material behavior.

Variety of structural flaws nucleate, extend and merge into different types of macroscopic damage without the need to use numerical "ingenuities" such as convenient mesh orientation, mesh reformulation or constant adoptive meshing. There is no need to develop constitutive laws or damage models in order to represent complex nonlinear responses of materials as they emerge naturally through the collective behavior of discrete units whose interaction is guided by relatively simple rules.

A summary of the CMD models that will be considered herein is shown in Figure 6.2 in conjunction with the natural spatial scale on which they are most commonly used.

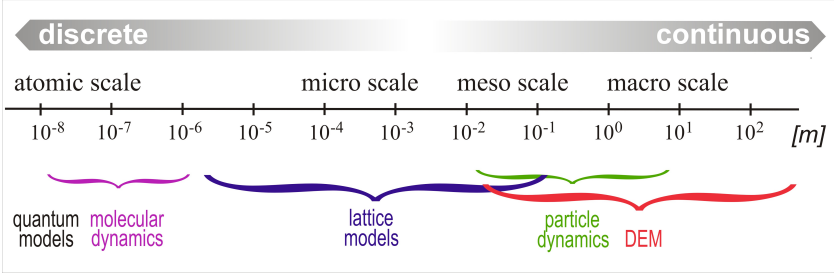

Figure 6.2: Spatial scales and corresponding traditional CMD models as tentatively classified herein for typical brittle materials with random microstructure (e.g., concrete).

It cannot be overemphasized that this classification is somewhat arbitrary, the boundaries between the models are hard to draw, and the associated length scales are subject to definition for each material separately. For example, the spatial scale corresponding to the meso-structure of concrete (of the order of centimeters or even decimeters as illustrated in Figure 6.1d) or rock massifs (of the order of decimeters or meters, Figure 6.1i) exceeds that of silicon carbide (SiC) by several orders of magnitude although they can all be classified the quasi-brittle systems.

With reference to Figure 6.2, on the nano-scale (e.g., the crystal lattice), it is possible to use the atomic models based on quantum mechanics. These rigorous methods[1] are based on the Schrödinger wave equation and semiempirical effective potentials which approximate quantum effects [1]. In contrast, classical MD relies on Newton's equations of motion and empirical potentials. Therefore, the traditional MD sacrifices the quantum mechanics rigor for the benefit of a much larger spatio-temporal modeling range. Observation scales and corresponding numerical models of mechanics of discontinua (conditionally divided into the three broad, intertwined categories: lattices, PD and DEM, as discussed above) correspond to concrete (Figure 6.1d) (inspired by [2]).

The MD refers to models where the basic building object is a point mass which may represent an atom, a molecule, a nanocluster, as well as a planet in a galaxy. In this short introduction, we always consider atoms (thus, the length scale in Figure 6.2) but, in general, it could be any of the above. From now on, the term MD, unless specified otherwise, is used for the traditional (classic) MD where each atom is treated as a point mass m_i (and, generally, a fixed charge q_i).

The term particle dynamics (PD), as used herein, designates "a coarse scale cousin to molecular dynamics" [3] sometimes also called the quasi-MD [4] to emphasize this kinship. It is developed to simulate phenomena on coarser spatial scales—the dynamic response of a material, either solid or fluid—based on a generalization of the MD modeling approach. The role of an atom is taken over by aggregates of atoms or molecules, represented by a material point called a "**continuum particle**" or a "quasi-particle". Depending on a particular application, this entity can represent, for example, a nanocluster, a ceramic grain, a concrete aggregate, a composite particle, a clastic rock granule and can, therefore, cover a wide range of spatial scales (up to the above-mentioned cosmological scales). Particle models use tried and tested MD techniques to directly confront various challenges of extremely complex physics. A critical step in the PD modeling is the transition from an adopted atomic potential to an interparticle potential (bottom-up approach) or a definition of an interparticle potential (a set of constitutive rules) on macro-scale (top-down), which is a common theme in all CMD numerical approaches. Traditional references for particle modeling are [4], [5], while [6] can be consulted for a review of recent developments.

Lattices are arguably the simplest CMD models (specifically, the spring-networks among them), comprised of one-dimensional discrete structural units such as springs, trusses or beams (Figure 6.3a,b). These elementary building units are assigned both geometric and structural properties and fracture characteristics that allow them to mimic elastic and inelastic deformation and fracture of the abstracted material. Lattice models could be

[1] So-called, "ab initio (first principle) MD", also known as "Born-Oppenheimer" or "Carr-Parrinello" MD.

considered meso-scale offshoots of both MD (micro-scale) but also the engineering truss and frame structures well-known from structural mechanics (macro-scale). Lattices were the original systems for modeling discontinuous media - various ideas of application in engineering mechanics date, at least, to Hrennikoff's pioneering work [7]. The modeling of network structures on a much coarser spatial scale than the atomic one eliminates the obvious need to work with a huge number of degrees of freedom, which could result in both computer congestion and data overload (so-called "data glut"), which would be inevitable if the atomic methods were used for modeling even the smallest structures on the macro-scale. This approach also reduces to a relatively modest level the number of nodes necessary to model the heterogeneity of the material structure. Comprehensive reviews of lattice models were published by Ostoja-Starzewski [3,8].

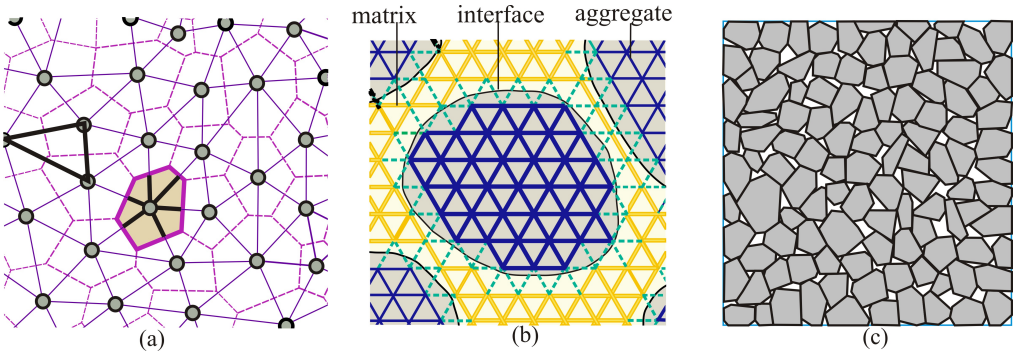

Figure 6.3: (a) Irregular triangular Delaney lattice dual to Voronoi grain thessalation. (b) Mesostructure of a three-phase composite projected on a regular triangular lattice. (c) Assembly of polygonal particles.

Unlike lattice models in which the basic structural elements are one-dimensional, in DEM (discrete element method) models the basic building blocks are typically of the same dimensionality as the considered problem. For example, planar DEMs include models of discontinuous systems comprised of 2D basic constituent elements such as circles, ellipses, or polygons (Figure 6.3c). These discrete elements are provided with geometric, structural, and contact properties that allow their "assemblies" (conglomerates, agglomerates) to approximate the complex phenomenological response of the subject material. In the most concise terms, DEMs enable the simulation of the motion and interactions of a huge number of discrete objects. It is important to note, that DEM unit blocks are actual geometric objects characterized by their dimension and shape, unlike the MD atoms, lattice nodal points, and particles (of PD) that are essentially material points. The macroscopic behavior of DEM models emerges as a consequent feature of the system derived from a small set of meso-properties of individual elements and their interactions. Contacts among discrete elements are endowed with the proscribed cohesive strength (including zero cohesive strength for non-cohesive, loose, material systems) and the ability to dissipate energy that allows representation of both elastic and inelastic phenomena and the nucleation of cracks and cooperative phenomena among them. It is important to emphasize that the properties of the contacts between discrete elements should be, in principle, identifiable based on the

material properties and the limited number of available experiments. Comprehensive DEM reviews were published in [9-11].

Regardless of the type of the CMD model, the evolution of a system of particles (the discrete structural elements in the most general sense) of known masses m_i, moments of inertia I_i, and positions r_i ($i = 1,2,\ldots,N$) is obtained by solving a system of equations of motion for each particle. Within classical mechanics, the equations that define the translational and rotational motion are those that correspond to Newton's second law

$$\begin{aligned} \frac{\mathrm{d}\mathbf{p}_i}{\mathrm{d}t} &= \frac{\mathrm{d}}{\mathrm{d}t}(m_i\dot{\mathbf{r}}_i) = \mathbf{F}_i, \\ \frac{\mathrm{d}\mathbf{L}_i}{\mathrm{d}t} &= \frac{\mathrm{d}}{\mathrm{d}t}(I_i\boldsymbol{\omega}_i) = \mathbf{M}_i \end{aligned} \tag{6.1}$$

where $\mathbf{p}_i$ and $\mathbf{L}_i$ mark, respectively, the linear and angular momenta of i-th particle and $\mathbf{F}_i$ and $\mathbf{M}_i$ corresponding forces and moments. Obviously, the motion of material points (all CMD systems except DEM) is completely defined by Equation $(6.1)_1$. (Hereinafter, symbols in boldface designate vectors and tensors.)

Lastly, the following brief introduction to CMD stems out of the two-part essay published in coauthorship with Antonio Rinaldi in "Handbook of Damage Mechanics: Nano to Macro Scale for Materials and Structures" [1]. Despite renewed efforts to make it as representative and comprehensive as possible, its content suffers unavoidably from the author's bias due to research backround and interests.

6.2 Molecular Dynamics

This short introduction aims to outline the basics of the traditional molecular dynamics (MD) method based on the classical mechanics. This computational simulation technique allows prediction of the temporal evolution of a system of material points (Figure 6.4) interacting via empirical interatomic potentials or molecular mechanics force fields by numerically solving Newton's equations of motion. Simulation methods based on quantum mechanics are beyond the scope of this overview, as well as many other advanced topics.

The first research article [12] in which Alder and Wainwright used MD to simulate perfectly elastic collisions of hard spheres was published in 1957. In 1960, Gibson and co-authors used a Born-Mayer potential to simulate a radiation damage of solid copper. Rahman (1964) simulated liquid argon by using 864 atoms interacting with a Lennard-Jones potential [13]. The first computer simulation of a simplified protein folding was produced in 1975 [14]. These pioneering articles were published more than half a century ago. Therefore, it is not surprising that many outstanding monographs devoted to computer simulations in condensed matter physics are available to the interested researcher (e.g., [5,15-17]).

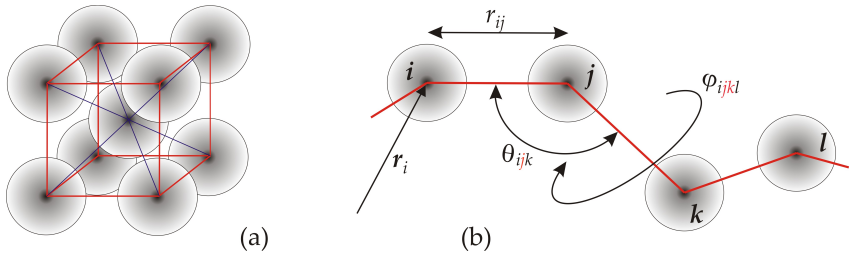

Figure 6.4: Schematic representation of two different solid structures: (a) the body-centered cubic crystal lattice, and (b) a molecular chain. The latter indicates 2-atoms (chemical bond), 3-atoms (angle bending), and 4-atoms (torsion; dihedral) interactions typical of the intramolecular bonding interactions.

The main feature of the MD method is the ability to analyze dynamics of (non)equilibrium processes with spatial resolution on the atomic scale. Thus, MD simulations play a role of computational microscope and have no computational alternative for many problems including atomic-scale phenomena that cannot be observed directly.

MD can be considered a numerical simulation offshoot of statistical mechanics. It has found research application in a wide range of problems prevalent in various scientific fields; such as, for example:

- Theoretical and statistical physics: fluid theory; properties of a statistical ensemble; structures and properties of small clusters; phase transitions,...
- Materials science and mechanics of materials: point, linear and plane defects in crystals and their interactions; stable and metastable structures of complex alloys and related phase diagrams; amorphous materials; radiation damage to materials; microscopic damage and fracture mechanisms; surface reconstructions; melting; growth of thin films; friction,...
- Biology, biochemistry and biophysics: molecular structure; chemical reactions; protein structure, functional mechanisms and folding process; drug design; vibrational relaxation and energy transfer; membrane structure; dynamics of biomolecules,... "Everything that living things do can be understood in terms of the jigglings and wigglings of atoms" [18].

6.2.1 Basic Idea of MD

The basic idea is simple. First, to setup the atomic system one must:

i) define a set of initial conditions (initial positions $\mathbf{r}_i$ and velocities $\mathbf{v}_i$ of all atoms in the system), then
ii) adopt the interatomic potential to define interatomic forces (internal forces), and finally
iii) introduce (externally applied) load acting on the system.

After that, the evolution of a system of atoms $(m_i, \mathbf{r}_i, \mathbf{v}_i)$ $(i = 1,2,\ldots,N)$ is determined by solving a system of equations of motion $(6.1)_1$ for each atom.

The resulting force acting on each atom at a given moment

$$f_{ij} = |\mathbf{f}_{ij}| = -\frac{\mathrm{d}\Phi}{\mathrm{d}r_{ij}}; \quad \mathbf{F}_i = -\sum_j f_{ij}\frac{\mathbf{r}_{ij}}{r_{ij}} \tag{6.2}$$

can be obtained from the interatomic potential Φ which is, in general, a function of the position of all atoms of the system ($r_{ij} = |\mathbf{r}_{ij}| = |\mathbf{r}_i - \mathbf{r}_j|$ being the intensity of the distance vector between the atoms i and j, that is, the interatomic distance, Figure (6.4b)). Thus, when the initial conditions and the interaction potential are defined, Equations $(6.1)_1$ can be solved numerically. Namely, the positions and velocities of all atoms of the system as a function of time are obtained as a result of solving a system of algebraic equations that approximates the system of differential Equations $(6.1)_1$. Thus, the motion of each individual atom (and each ensemble of atoms) is completely deterministic. In most cases, analysts are not interested in the trajectories of individual atoms but in the macroscopic properties of materials that result from the motion of a multitude of atoms. The information resulting from computer simulations can be averaged at certain time intervals for all (or selected) atoms of the system to obtain thermodynamic parameters (Chapter 6.2.4).

6.2.2 Empirical Interatomic Potentials

Empirical potentials used in materials science and mechanics of materials are called interatomic potentials. The role of interatomic forces (6.2) is crucial since the MD simulation is realistic only insofar as the interatomic forces are similar to those operating between real atoms in the corresponding atomic configuration [16]. As already noted, the classical definition of interatomic interaction, based on empirical potentials, represents the rigorous quantum mechanical nature of materials in a limited way through impromptu approximations.

The interatomic potentials depend on the states of the electrons, thus, the electrons are the origin of the interatomic forces. Nonetheless, the electrons are not directly present in the traditional MD model – their influence is introduced indirectly through analytical functions that define potential energy solely on the basis of the atomic (nuclei) positions (6.3). The creation of the analytical function of potential energy and the choice of input parameters is often based on the fitting of the available experimental data that are of greatest interest for the specific problem being studied (e.g., modulus of elasticity, cohesive energy, phase transition temperature, vibration frequencies).

When forming an MD model, the interatomic potential is adopted either on the basis of knowledge of the atomic nature of the simulated material or a priori. The construction of interatomic potential is as much an art as it is a science, but from the point of view of users, the choice is, nowadays, quite simplified thanks to the available literature. This choice is essential not only because the adequacy and accuracy of the potential dictate the quality of the simulation results but also due to the fact that its complexity determines the efficiency of the code in terms of simulation duration. Although some compact potentials may seem inadequate, many fundamental, generic aspects of a physical phenomenon can be observed thanks to the advantages provided by their simplicity.

The empirical interatomic potential

$$\begin{aligned}\Phi &= \Phi(r_1, r_2, \ldots, r_N) = \\ &= \sum_i \Phi_1(r_i) + \sum_i \sum_{j>i} \Phi_2(r_i, r_j) + \sum_i \sum_{j>i} \sum_{k>j>i} \Phi_3(r_i, r_j, r_k) + \cdots\end{aligned} \tag{6.3}$$

represents the potential hypersurface of the non-bonded interactions [5]. In expression

(6.3), the terms $\Phi_1, \Phi_2, \Phi_3, \ldots$ are, respectively, contributions due to external fields (e.g., gravitational or the container wall), pair, triple and higher order interatomic interactions. In traditional MD, rigor is often sacrificed for the sake of efficiency, and interatomic interactions among all atoms have been replaced by less computer-intensive approximations in which each individual atom interacts only with a certain number of **nearest neighbors** (so-called, first-nearest, second-nearest, etc.). Further, by neglecting the three-body interactions (involving interatomic angles) and higher, the potential energy of the system can be approximated by the sum of isolated empirical biatomic potentials (**pairwise additivity** assumption)

$$\Phi = \frac{1}{2}\sum_i \sum_j \phi(r_{ij}). \tag{6.4}$$

It is obvious that the concept of pairwise additivity (6.4) represents a huge simplification with far-reaching consequences. For some crystal lattices, the pairwise interaction is not able to take into account a good portion of the cohesive interaction [19]. Furthermore, the interaction in ionic crystals may be a consequence of the polarization effects, attributed to the action of the electric fields of the surrounding ions, which cannot be described by simple pair potentials. However, the main interactions in the ionic and Van der Waals crystal lattices are believed to be essentially pairwise [19]. Many more complex forms of potential can be used as needed at the cost of increasing the duration of the simulation. The consequence of choosing the central-force potential (6.4) is that the total energy of the system is conserved. In the language of statistical physics, classical MD generates a microcanonical ensemble (N, E, V).

The **pair potentials** are the simplest potentials since the force of interaction of two atoms is completely determined by their mutual distance. There is an extensive literature on the ways in which these potentials are experimentally determined or theoretically modeled (e.g., [20]). Strictly speaking, they realistically describe only noble gases. The simplest potential of this type is the discontinuous potential of a "rigid sphere" which implies that the value of the interatomic force is equal to either: (i) zero, if the interatomic distance is greater than the prescribed value; or (ii) infinity, if the interatomic distance is equal to or less than the prescribed value.

A more realistic interatomic interactions are obtained under the assumption that the interaction force gradually varies from strongly repulsive (at small interatomic distances) to attractive (at medium distances) until it finally converge asymptotically to zero (with further increase in distance) (Figure 6.5). The best known potential of this type, which has been widely used in the past when the focus of research was on the study of qualitative trends (essential physics) rather than narrowly specific issues, is the **Lennard-Jones 6-12 potential**

$$\phi_{ij} = -\varepsilon_{LJ}\left[2\left(\frac{1}{\bar{r}_{ij}}\right)^6 - \left(\frac{1}{\bar{r}_{ij}}\right)^{12}\right] \tag{6.5}$$

originally developed for noble gases from van der Waals cohesion [21]. In expression (6.5), ε_{LJ} represents the depth of the potential well, and $\bar{r}_{ij} = (r/r_0)_{ij}$ ratio of current and equilibrium distance between atoms i and j (Figure 6.5). These model parameters are chosen with the aim of optimally reproducing the most desirable physical and mechanical

properties of the material. The amount of published work with Leonard-Jones systems since the creation of MD is unsurpassed by any other potential, and only for that reason, not to mention others, its importance cannot be overemphasized. However, it can be ill-advised to apply this potential for the quantitative study of more complex materials.

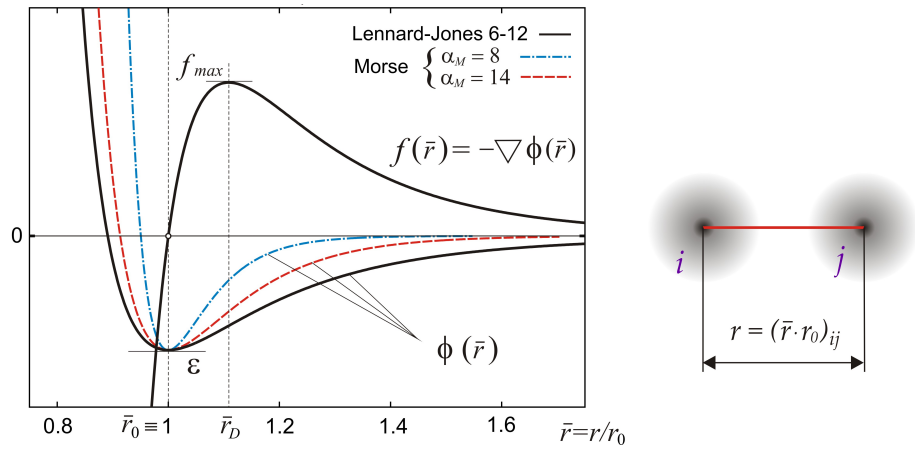

Figure 6.5: Schematic representation of pair potentials with unit depth of the **potential well**: Lenard-Jones 6-12 with corresponding force (solid black line), Morse for two parameter values α_M which define the width of the potential well. These curves illustrate the atomic hypothesis that „all things are made of atoms—little particles that move around in perpetual motion, attracting each other when they are a little distance apart, but repelling upon being squeezed into one another" [18].

The term $\bar{r}_{ij}^{-12}$ in (6.5), which dominates the interatomic repulsion, is selected for application convenience: as far as the physics is concerned, the exponential term is a more appropriate choice. The simplest potential that takes this into account is the Morse potential:

$$\phi(\bar{r}_{ij}) = \varepsilon_M \left\{ \exp[-2\alpha_M(\bar{r}_{ij} - 1)] - 2\exp[-\alpha_M(\bar{r}_{ij} - 1)] \right\}$$

The adoptable parameter α_M defines the slope of the repulsive wall (that is, the width of the potential well; Figure 6.5). The parameters ε_M, r_0 and α_M are, as in the previous case, usually determined by fitting the material properties that are most relevant to the problem being analyzed. The Morse potential was originally developed for covalent bonds that are strongly spatially oriented, so the interatomic distance is not sufficient for a realistic description of the interaction [22]. Although the inverse-power form of the interatomic potential (6.5) is most often used in heuristic studies, the results of quantum mechanical calculations, as already mentioned, favor the exponential form, which is later used in some particle models (6.26).

If electrostatic charges are present, it is necessary to add the appropriate Coulomb potentials

$$\phi(r_{ij}) = \frac{q_i q_j}{4\pi\bar{\varepsilon}_p r_{ij}}$$

where q_i and q_j are charges, and $\bar{\varepsilon}_p$ the permittivity.

The simple potentials also provide a direct way to estimate the modulus of elasticity and the theoretical strength using expressions

$$E = \frac{1}{r_0}\left(\frac{\mathrm{d}^2\phi}{\mathrm{d}r^2}\right)\Bigg|_{r=r_0}, \quad \sigma_m = \frac{1}{r_0^2}\left(\frac{\mathrm{d}\phi}{\mathrm{d}r}\right)\Bigg|_{r=r_D} \tag{6.6}$$

which follows from its physical nature [23]. In Equation $(6.6)_2$, r_D stands for the so-called separation distance defined by the maximum value of the interatomic force $\mathrm{d}f(r)/\mathrm{d}r = 0$, that is, the inflection point of the interparticle potential $\mathrm{d}^2\phi(r)/\mathrm{d}r^2 = 0$ (Figure 6.5).

The basic purpose of any interatomic potential is to correctly reproduce the most prominent characteristics of atomic bonds. Therefore, it should always be borne in mind that the pair of potentials were "originally developed to describe atomic interaction in systems in which these forms of potentials are physically justified" [24] and resist the temptation to use them injudiciously for their simplicity.

The pair potentials cannot accurately describe interatomic interactions in more complex systems [16] such as, for example, strongly covalent systems (e.g., SiC), most ceramics characterized by fully populated orbitals, metals characterized by delocalized "sea of electrons", or semiconductors. However, in MD simulations from the 1950s to the 1980s, a couple of these simplified potentials were used almost exclusively. Significant progress was made during the 1980s with the development of **many-body potentials** for metals based on the concept of atomic density (e.g., [25]). The main observation that needed to be modeled was that interatomic bonds become weaker when nested in a "dense" local environment. Accordingly, the force acting on an atom depends not only on the distance separating its nucleus from nuclei of its neighbors, but also on the local atomic density. In other words, the forces between ions are characteristically dependent on many bodies ("many-body in character"), instead of simply being pairwise additive. The focus is usually on the attractive part of the potential [16]. Accordingly, the so-called "glue model" potentials have been developed (e.g., [26] and references cited therein). Among these potentials, the best known is the so-called **embedded atom method** (**EAM**)

$$\begin{aligned} \Phi(r_{ij},\rho_i) &= \frac{1}{2}\sum_i\sum_{j=i}\phi(r_{ij}) + \Psi = \sum_i\left[\frac{1}{2}\sum_{j\neq i}\phi(r_{ij}) + \psi(\bar{\rho}_i)\right], \\ \bar{\rho}_i &= \sum_{j\neq i}\rho(r_{ij}). \end{aligned} \tag{6.7}$$

developed to approximate the interaction between ions in metals. The various forms of (6.7) differ from each other only in the forms of functions: ϕ (pairwise term depending entirely on the interatomic distance), ψ (density-dependent contribution - the embedding energy necessary to insert the i-th atom into the background of the electron density $\bar{\rho}_i$), and ρ_{ij} (atomic density function) [26].

Differences between pair potentials and many-body potentials have been discussed in detail in the literature (e.g., [27], [28]). EAM potential has been used extensively to model ductile metals.

Finally, empirical potentials in organic chemistry and molecular biology are often called force fields. It should be noted that for complex macro-molecular chains (e.g.,

synthetic polymers, biopolymers), in addition to non-bonding forces (van der Waals and electrostatic), it is necessary to consider the **intramolecular bonding interactions** illustrated in Figure 6.4b. The elementary models of this kind include contributions due to:

(i) bond stretching: 2-atoms vibrations about the equilibrium bond length $(6.8)_1$
(ii) angle bending: 3-atoms vibrations about the equilibrium angle they define $(6.8)_2$

$$\frac{1}{2}\sum_{\text{bonds}} k_{ij}^{\alpha}\left(r_{ij}-r_{0ij}\right)^2, \quad \frac{1}{2}\sum_{\text{bend angles}} k_{ijk}^{\beta}\left(\theta_{ijk}-\theta_{0ijk}\right)^2, \tag{6.8}$$

(iii) torsion (dihedrals, proper and improper, 4-atoms torsional vibrations), and
(iv) various cross-terms [29].

These so-called bonded interactions are not further discussed in this introduction. The details are available in [29], [30].

Further considerations of empirical potentials go beyond the objectives of this introduction and can be found in literature (e.g., [24], [30]; and many others). In the last thirty years, empirical potentials have been developed in a targeted way - for specific material systems with a range of applicability in mind. The ultimate test of any empirical potential is its success in simulating properties of interest. However, it seems appropriate to conclude this brief review by adding that in the constant competition between the more sophisticated and the spatially larger MD models, under the constraints imposed by computational capabilities, the latter are still considered more advisable in terms of meaningful results. In other words, it is generally accepted that it is better to increase the size of the MD system and simplify the potential, than to do the opposite. This trend has resulted in the development of parallel processing [11], [31], [32] without which MD simulations in the contemporary research cannot be imagined.

Shortening the range of potential

The empirical potentials presented in Chapter 6.2.2 have an unlimited range. In MD simulations, it is a common custom to establish the cut-off distance (r_{cut}) and to neglect interatomic interactions for distances that exceed it because the corresponding forces are insignificant (Figure 6.5). This neglect of interatomic action in the range of potential asymptotic approach to zero leads to program simplification and huge computational savings due to a drastic reduction in the number of interacting atomic pairs.

However, a simple shortening of the potential would lead to a new problem: whenever the mutual distance between pairs of atoms "crossed" over the cutting distance, there would be a small, abrupt change in the energy of the system. A large number of such events could, on the one hand, have an impact on the law of conservation of energy, and on the other, affect the physics of subtle micro-processes that depend on the details of the local energy state. Therefore, limiting the range of potentials is most often done by a smooth transition in the attractive range, for example, by using a cubic spline. As an example, the approach of Holian et al. [27] is based on the Lennard-Jones potential (6.5) interrupted at $r_{spl} \approx 1.109 r_0$ and replaced by the cubic spline in r^2

$$\phi_{spl}(r) = -\mathscr{A}(r_{cut}^2 - r^2)^2 + \mathscr{B}(r_{cut}^2 - r^2)^3$$

which reaches zero at r_{cut}. The spline parameters are chosen to ensure continuity of coordinates, inclination and curvature ($C0$, $C1$, and $C2$) at the point of intersection ($r = r_{spl}$):

$\phi_{LJ} = \phi_{spl}$, $\phi'_{LJ} = \phi'_{spl}$ and $\phi''_{LJ} = \phi''_{spl}$. Note that, since the cubic spline is defined in r^2 instead of r, rooting and division operations with r are avoided in the MD simulation, while differences in the appearance of the function are often practically imperceptible [27].

Physical quantities are, of course, somewhat influenced by this shortening of the range of potentials. Overall, the eventual assessment of these effects is a problem specific to each application (e.g., [16], [17]).

6.2.3 Integration Algorithms

The core of the MD program is the integration algorithm necessary for the integration of the equations of motion $(6.1)_1$. These algorithms are based on the finite difference method in which time is discretized within a finite network and the time step, δt, represents the distance between successive points on the network. Knowing the position and some of its time derivatives in the current time (t), allows calculation of the same quantities in the next time $(t+\delta t)$. In addition to being as accurate as possible, the integration algorithm should be both fast and of modest memory requirements, to allow the application of the longest possible time step, and to be simple for implementation.

Several different methods are available for this purpose but only one will be discussed herein. The **Verlet algorithm** is still the most widely used, although more powerful techniques for integrating finite difference equations are available. The derivation of this algorithm is based on the development of the atomic position function in the Taylor series at an arbitrary time t

$$\mathbf{r}_i(t+\delta t) = \mathbf{r}_i(t) + \mathbf{v}_i(t)\delta t + \mathbf{a}_i(t)\delta t^2 + \frac{\mathrm{d}^3\mathbf{r}(t)}{\mathrm{d}t^3}\delta t^3 + O(\delta t^4)$$

that is

$$\mathbf{r}_i(t-\delta t) = \mathbf{r}_i(t) - \mathbf{v}_i(t)\delta t + \mathbf{a}_i(t)\delta t^2 - \frac{\mathrm{d}^3\mathbf{r}(t)}{\mathrm{d}t^3}\delta t^3 + O(\delta t^4).$$

Adding the previous two expressions yields

$$\mathbf{r}_i(t+\delta t) + \mathbf{r}_i(t-\delta t) = 2\mathbf{r}_i(t) + 2\mathbf{a}_i(t)\delta t^2 + O(\delta t^4).$$

The time-reversible equation for calculating the next position has the form

$$\mathbf{r}_i(t+\delta t) = 2\mathbf{r}_i(t) - \mathbf{r}_i(t-\delta t) + \delta t^2 \sum_{j\neq i} \frac{\mathbf{f}_{ij}(\mathbf{r}_i, \mathbf{r}_j)}{m_i} + O(\delta t^4). \tag{6.9}$$

This method of integration is very compact and easy to implement. Since no dissipative forces act between the atoms, the dynamic system is conservative. Therefore, the force by which the atom j acts on the atom i is $f_{ij} = -\nabla_i \phi(r_{ij})$, and its calculation is by far the most demanding part of MD simulations. The Verlet method seems to be the least time-consuming and thus the most suitable for modest computing resources, which explains its popularity. The main disadvantages of the Verlet algorithm are clumsy handling of velocities

$$\mathbf{v}_i(t) = \frac{\mathbf{r}_i(t+\delta t) - \mathbf{r}_i(t-\delta t)}{2\delta t} + O(\delta t^2)$$

which requires knowledge of the next position $r_i(t+\delta t)$ and is susceptible to rounding error due to relatively large residue $O(\delta t^2)$. However, it is possible to obtain more accurate estimates of the velocity (and thus the kinetic energy of the system) using various modifications of the Verlet algorithm.

The Störmer algorithm is a such modification of the Verlet algorithm, where the most pronounced computational advantage stems from the fact that at no time is the difference between two large numbers used to calculate a small number [5]. The computational scheme has the form

$$\mathbf{r}_i(t+\delta t) = \mathbf{r}_i(t) + \delta t\, \mathbf{v}_i\left(t+\frac{\delta t}{2}\right). \tag{6.10}$$

In addition to current positions and accelerations, recorded quantities include mid-step speeds

$$\mathbf{v}_i\left(t+\frac{\delta t}{2}\right) = \mathbf{v}_i\left(t-\frac{\delta t}{2}\right) + \delta t\, \mathbf{a}_i(t). \tag{6.11}$$

Since the Störmer algorithm is only a modification of the Verlet algorithm, it produces identical trajectories. The problem, evident in expressions (6.10), arises because the velocities are not calculated at the same time points as their positions, which complicates the calculation of the total energy of the system.

The above-mentioned algorithms, and similar ones available in literature, are completely adequate for most MD simulations. However, it is sometimes necessary to use higher-order integration schemes which use higher-order position vector derivatives in the Taylor approximation. These algorithms not only achieve higher calculation accuracy for the same time step but also allow use of a longer time step without losing accuracy (at least in a short run). Unfortunately, the use of these higher-order algorithms (an example is the popular predictor-corrector method) is coupled with many implementation difficulties that go beyond the scope of this introduction and have been discussed in detail in the literature (e.g., [5], [17]).

6.2.4 Calculation of Macro-parameters of State

Statistical physics provides the connection between microscopic behavior of the system and the macroscopic world described by thermodynamics. In order to calculate a certain physical parameter of the state of a macroscopic system (such as stress, strength, temperature, damage) it is necessary to define it as a function of the raw MD output data (that is, the atomic positions, velocity and forces ($\mathbf{r}$, $\mathbf{v}$, $\mathbf{a}$)). Strictly speaking, this can be achieved only when the thermodynamic system is: (i) large enough to be statistically homogeneous, and (ii) either in equilibrium or close enough to equilibrium (measured by the Deborah number [33]). If these preconditions are not met, the meaning of the continuum concepts becomes disputable.

Stress, strain and effective stiffness

The elastic strain energy of the system in the (proximity of) equilibrium can be developed in the Taylor series [34]

$$\begin{aligned} U &= U_0 + \frac{1}{1!}\frac{\partial U}{\partial \varepsilon_{\alpha\beta}}\varepsilon_{\alpha\beta} + \frac{1}{2!}\frac{\partial^2 U}{\partial \varepsilon_{\alpha\beta}\partial \varepsilon_{\gamma\delta}}\varepsilon_{\alpha\beta}\varepsilon_{\gamma\delta} + \cdots = \\ &= U_0 + \sigma_{\alpha\beta}\varepsilon_{\alpha\beta} + \frac{1}{2}C_{\alpha\beta\gamma\delta}\varepsilon_{\alpha\beta}\varepsilon_{\gamma\delta} + \cdots \end{aligned} \tag{6.12}$$

In the (proximity of) equilibrium state, the resultant forces acting on any atom of the system $(6.2)_2$ are (close to) zero, which implies that each atom lies in its potential well. Such system must be, by definition, stable in the event of an infinitesimal disturbance, such as the one imposed by the homogeneous strain tensor $\varepsilon_{\alpha\beta}$ acting as an external load.

The linear (second) term in the Taylor series (6.12) represents the stress tensor. It is important to note that this is a general thermodynamic relation independent of the applicability of Hooke's law [35]. With regards to the potential energy of a system, if the interatomic actions can be successfully approximated with the EAM (6.4), the stress tensor components are

$$\sigma_{\alpha\beta} = \frac{1}{2\bar{V}N}\sum_{\substack{i,j \\ j\neq i}}\frac{\mathrm{d}\phi}{\mathrm{d}r_{ij}}\frac{(r_{ij})_\alpha (r_{ij})_\beta}{r_{ij}} + \frac{\mathrm{d}\Psi}{\mathrm{d}\bar{V}}\delta_{\alpha\beta} = -\frac{1}{2\bar{V}N}\sum_{\substack{i,j \\ j\neq i}} f_{ij}\frac{(r_{ij})_\alpha (r_{ij})_\beta}{r_{ij}} + \frac{\mathrm{d}\Psi}{\mathrm{d}\bar{V}}\delta_{\alpha\beta} \tag{6.13}$$

where $\bar{V}$ is the average volume per atom, while $(r_{ij})_\alpha$ and $(r_{ij})_\beta$ are corresponding (α and β) projections of the distance vectors $\mathbf{r}_{ij}$ [35], [36]. Since the stress definition (6.13) is inherently related to the static equilibrium state, it is, strictly speaking, applicable only to static (or quasi-static) deformation where the resultant force acting on each atom $(6.2)_2$ are equal (or "close enough") to zero. On the other hand, dynamic deformation implies wave propagation and, in order for expression (6.13) to be applicable, it must be tacitly assumed that the nonequilibrium process can be represented by a successive series of equilibrium processes. This concept is routinely used, out of necessity, in thermodynamics of nonequilibrium processes.

The third term in the Taylor series (6.12) defines the elastic stiffness tensor

$$\begin{aligned} C_{\alpha\beta\gamma\delta} = {} & \frac{1}{2\bar{V}N}\sum_{\substack{i,j \\ j\neq i}}\left(\frac{\mathrm{d}^2\phi}{\mathrm{d}r_{ij}^2} - \frac{1}{r_{ij}}\frac{\mathrm{d}\phi}{\mathrm{d}r_{ij}}\right)\frac{(r_{ij})_\alpha (r_{ij})_\beta (r_{ij})_\gamma (r_{ij})_\delta}{r_{ij}^2} - \\ & - \frac{1}{2}\frac{\mathrm{d}\Psi}{\mathrm{d}\bar{V}}\left\{(\delta_{\alpha\gamma}\delta_{\beta\delta} + \delta_{\beta\gamma}\delta_{\alpha\delta})(2-\delta_{\alpha\beta}) - \frac{1}{2}\delta_{\alpha\beta}\delta_{\gamma\delta}(4-\delta_{\alpha\gamma}-\delta_{\beta\gamma}-\delta_{\alpha\delta}-\delta_{\beta\delta})\right\} + \\ & + \bar{V}\frac{\mathrm{d}^2\Psi}{\mathrm{d}\bar{V}^2}\delta_{\alpha\beta}\delta_{\gamma\delta} \end{aligned} \tag{6.14}$$

In the case of pair potentials (6.4), $\Psi = 0$ and only the first terms of Equations (6.13) and (6.14) remain. When the EAM (6.7) or related methods are used to model interatomic interactions, it is necessary to use the complete Equations (6.13) and (6.14) that take into account the density (the average volume per atom) dependence of the potential [24].

The strain tensor components are calculated based on the deviation of the current network configuration from the reference configuration defined at the initial moment. Since atomic positions are known at all times (therefore, in both the initial and the current configuration), calculating the strain components is a straightforward task. For example, the components of the left Cauchy-Green strain tensor, corresponding to i-th atom of the plane system, are commonly (e.g., [37]) defined as follows

$$b_{\alpha\beta} = \frac{1}{3}\sum_{j=1}^{6}(\bar{r}_{ij})_\alpha\,(\bar{r}_{ij})_\beta, \quad (\bar{r}_{ij})_\alpha = (r_{ij})_\alpha / r_0. \tag{6.15}$$

It should be noted that, unlike the stress definition (6.13), the virial equation (6.15) is instantaneously valid in time and space, that is, it does not require time averaging.

Temperature

The temperature evaluation during dynamic processes raises some fundamental questions related to the thermodynamics of nonequilibrium processes in relation to basic thermostatic concepts such as entropy and absolute temperature of nonequilibrated systems (e.g., [34], [38], [39]). That discussion is bypassed herein. It is deemed sufficient just to point out the Callen's [40] claim that the nonequilibrium definitions of entropy and temperature are based on uncertain premises. Be it as it may, a consensus has been reached, over time, on the use of a standard definition of temperature, known from the kinetic theory of gases. This definition is based on the equipartition theorem that provides a relationship between the average kinetic energy and the instantaneous kinetic temperature of the system: atomic velocities establish a thermometer. According to this theorem, each degree of freedom contributes $k_B T/2$ to the internal energy of the system from where it follows

$$T \equiv \frac{2}{3k_B}\langle E_k\rangle = \frac{2}{3k_B}\left\langle \frac{mv^2}{2}\right\rangle. \tag{6.16}$$

where k_B is the Boltzmann constant. The definition (6.16) is firmly established in statistical mechanics as it derives from the distribution of the highest probability of a canonical (N, V, T) ensemble [34], [41]. Thus, expression (6.16) tacitly implies that the system is thermally equilibrated, and the atomic velocities distributed in accordance with the **Maxwell-Boltzmann distribution** (6.17) [42]. As argued by Holian and coworkers [39], the instantaneous kinetic temperature is the only meaningful definition in nonequilibrium situations.

Importantly, the intensity of velocity vector $\mathbf{v}(v_x, v_y, v_z)$ appearing in Equation (6.16) corresponds to the vibratory motion and, therefore, does not contribute to the resultant momentum. Nonetheless, it possesses a finite kinetic energy that is identified with the thermal energy and is related to the absolute temperature in MD simulations. With reference to Figure 6.6a, the vibrational velocity components could be obtained by subtracting the velocity of correlative (systematic) motion (full black line) from the total (individual) atomic velocity (dashed red line). The total velocity of each atom is obtained directly by solving Newton's equations of motion $(6.1)_1$. The associated velocity of correlative motion can be calculated by spatially averaging the total velocities of all atoms belonging to a particular averaging region centered at the atom in question (Figure 6.6b). This averaging

volume (surface in 2D) plays a role of a virtual sensor (thermometer in this case). This approach is reminiscent of the division of the motion of molecules, in the kinetic theory of gases, into a "random" and a "systematic" part [44].

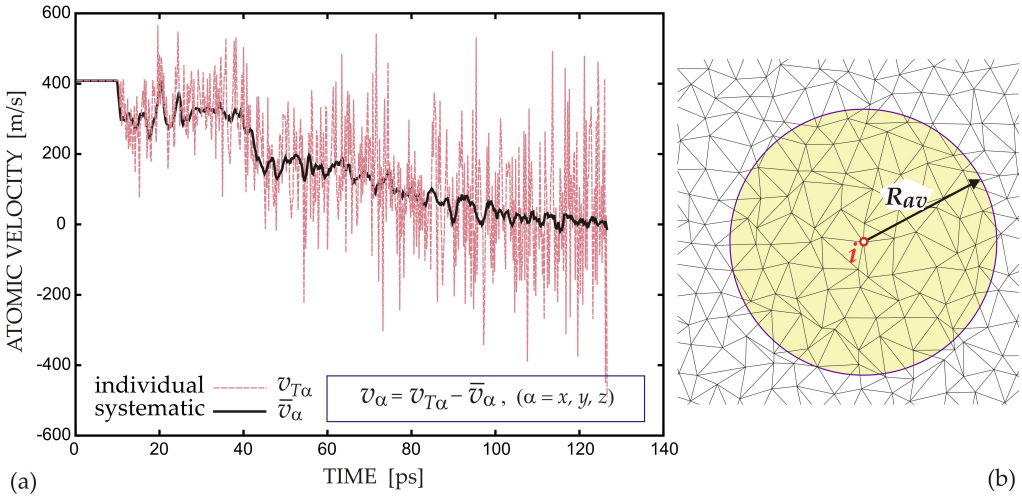

Figure 6.6: (a) A typical time history of atomic speed recorded in the course of 0.408 [km/s] ballistic Taylor test [45]. The full black line represents the systematic velocity of (correlative) motion while the dashed red line represents the corresponding total velocity of the individual atom. The difference between the total velocity and the associated systematic velocity results in the velocity of vibratory motion which defines the thermal energy of random vibrations related to the instantaneous kinetic temperature (6.16) (Adopted from [43]). (b) Averaging area (in general, volume) superimposed on an irregular lattice for evaluation of the macroscopic state parameters in MD simulations (**virtual sensor**).

The instantaneous kinetic temperature (6.16) is averaged in both time and space. In 2D simulations, the averaging area is usually taken to be the same circular region (shaded in Figure 6.6b) that was previously used to calculate the correlative motion velocity. Therefore, each node in the network also represents the center of the averaging area of radius R_{av}, characterized by the corresponding velocity of correlative motion and the temperature obtained by averaging within the specified area. The size of the averaging region is the result of a compromise between contradictory requirements for the largest possible size of statistical sample and the finest possible calculation (measurement) resolution. An example of the arrangement of the averaging regions is shown in Figure 6.7 for the case of a slender flat-head projectile hitting a rigid wall (the Taylor ballistic test [45]). The circular averaging areas (6.6b), which play the role of measuring gages, follow the movement of the atoms on which they are centered during the sample deformation. Accordingly, if during deformation the atoms, on which the averaging surfaces are centered, approach the edge of the deformed object, incomplete averaging may occur, which has different consequences for different macroscopic parameters (depending on their definitions; Equations (6.13)-(6.15)) which should be carefully examined in each specific case.

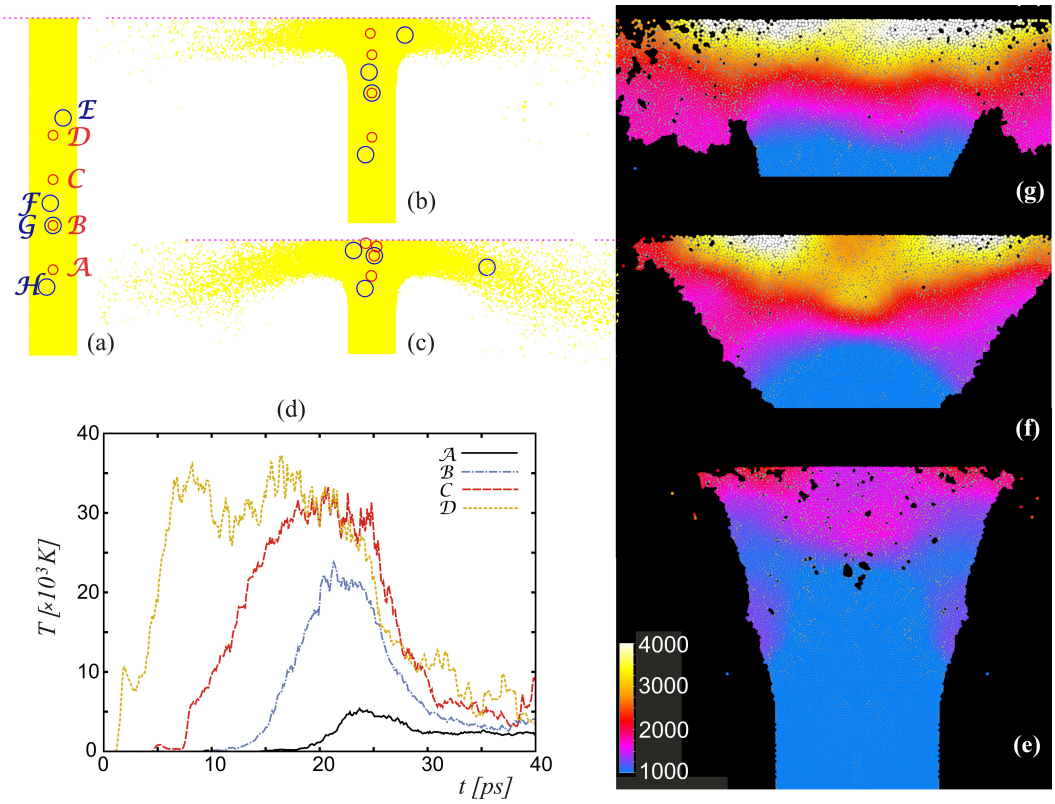

Figure 6.7: Temperature evolution for the simulation of the Taylor ballistic test (the (nano)projectile collision with the rigid wall). (a-c) Sequence of deformed nanoprojectile configurations upon $v_{imp} = 7$[km/s] rigid-wall collision with the marked positions of the eight averaging areas ("measurement gages") used to evaluate the macroparameters of state: (a-c) 0.2[ps], 6[ps], 12[ps], respectively (Adopted from [46]). (d) An example of time histories of temperature recorded at four measurement locations $A-D$ equidistantly distributed along the longitudinal axis of symmetry of the nanoprojectile at the impact velocity $v_{imp} = 4$[km/s] (Adopted from [43]). (e-g) Examples of temperature field evolutions during the $v_{imp} = 0.7$[km/s] simulation; the images correspond 10[ps], 20[ps], and 50[ps], respectively. The scale of values on the label refers to the absolute temperature in degree Kelvin.

Thermal initialization of the system

Assignments of the initial and boundary conditions necessary for an MD simulation imply definition of the initial positions and initial velocities of all atoms of the system. The vibrational part of the initial velocities are generally defined by selecting the velocity intensities for each atom from the Maxwell-Boltzmann distribution for the desired initial sample temperature (T_0) while the velocity directions are assigned randomly.

The Maxwell-Boltzmann distribution of the vibrational velocities provides the probability density for atoms with the velocity intensity v and has the form

$$pdf(v) = 4\pi \left(\frac{m}{2\pi k_B T_0} \right)^{3/2} v^2 \exp\left(-\frac{mv^2}{2k_B T_0} \right). \tag{6.17}$$

Figure 6.8 illustrates the Maxwell-Boltzmann velocity intensity distribution for tungsten (W) at temperatures of 300 [K] and 1000 [K]. As can be seen, the distribution is not symmetric: the average value of the velocity intensity $(6.18)_1$ is always greater than the most probable value $(6.18)_2$ (corresponding to the maximum of the distribution curve)

$$\langle v \rangle = \sqrt{\frac{8k_B T_0}{\pi m}}, \quad v_m = \sqrt{\frac{2k_B T_0}{m}} = \frac{\sqrt{\pi}}{2}\langle v \rangle. \tag{6.18}$$

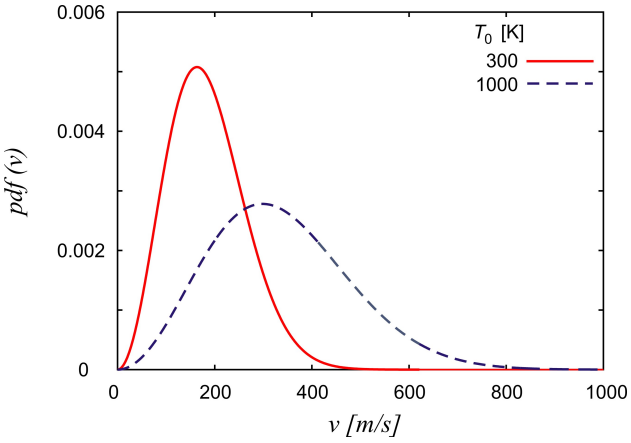

Figure 6.8: The Maxwell-Boltzmann speed distributions for tungsten for two different temperatures.

6.2.5 MD Simulation Cell and List of Neighbors

The response of small systems can be dominated by surface effects that may obscure the physical response of the bulk material. A simulation cell with **periodic boundary conditions** (Figure 6.9) is introduced to eliminate these contaminating surface effects whenever it is of interest to study behavior of the bulk material. The volume (surface area in 2D) of a periodic cell is representative of bulk material in the sense that it is considered to be composed of periodic cells surrounded on all sides by their exact replicas [5] as illustrated in Figure 6.9. This periodicity implies that the atom, in the bottom-right cell corner of Figure 6.9, leaving the MD simulation cell instantaneously reappears at the bottom-left cell corner.

This elimination of unwanted surface effects using these periodic cells is achieved at the cost of introducing non-physical periodicity into the atomic system. Adverse consequences include: (i) unrealistically rigid response, (ii) unnatural wavelengths in the solution fields, (iii) suppression of localization that might otherwise occur [47], and (iv) violation of the conservation of angular momentum [15].

In order to simulate the most general loading conditions, it is necessary to be able to change the shape and size of the periodic cell and maintain constant values of certain state parameters (typically, temperature or pressure; the NTP ensemble). The restriction that the shape of the periodic cell must remain unchanged has a negative impact on the applicability

of the periodic cell. Therefore, several alternative MD methods have been proposed as potential solutions for above mentioned problems in a series of papers [48]-[51]. In these studies, the shape of a periodic cell is treated as a phenomenological variable subject to change over time.

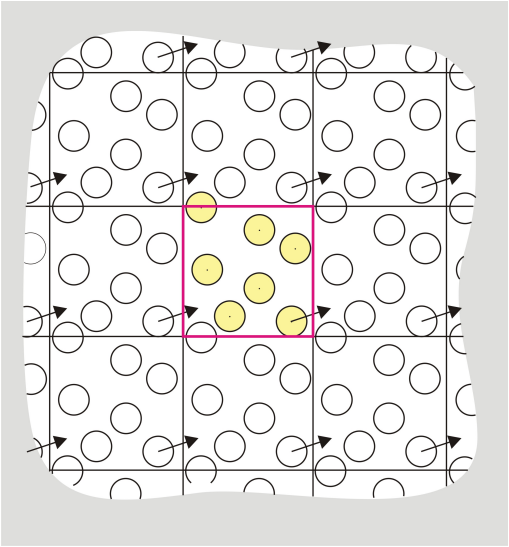

Figure 6.9: Periodic boundary conditions and the simulation cell.

The time required to calculate the interactions between the N atoms of a 2D system using algorithm (6.9) is proportional to N^2 [5]. In order to improve the speed of program execution, it is very useful to maintain a **list of neighbors** of each atom that Verlet originated in his classic work [52]. For example, the list of neighbors of the i-th atom is formed by including all atoms at a distance less than the prescribed cut-off distance. Between periodic updates of the neighbor list (typically, several calculation cycles), the program does not check all other atoms in the system but only those that appear in the list for a given atom.

6.2.6 Temperature and Pressure Control

In the absence of dissipative forces, the equation of motion of classical mechanics results in the conservation of the total energy of the system which corresponds to a microcanonical (N, V, E) ensemble. The calculated temperature (6.16) and pressure in the standard MD formulation are not constrained and can vary significantly during the simulation (Figure 6.7). Most often, it is of utmost importance to evaluate these temperature and pressure changes. On the other hand, sometimes it is of interest in MD simulations to constrain temperature or pressure or both. The importance of temperature and pressure control has made the topics of virtual thermostats and barostats very popular among researchers, resulting in an abundance of different methods (e.g., [53]-[55]).

Nose-Hoover thermostat

Atomic velocities establish a thermometer, as argued in Chapter 6.2.4. All algorithms performing the role of thermostat use some modifications of Newton's second law of motion to provide a constant average temperature of the particle ensemble by adding and removing its energy [55]. The temperature control is illustrated here by the Nose-Hoover algorithm as formulated by Holian and co-authors [39].

The Nose-Hoover thermostatted MD has a theoretical basis in the classical thermodynamic concept of "connecting" a thermodynamic system (in this case, the MD cell) with a heat reservoir that ensures a constant temperature during the simulation. Consequently, the given atomic ensemble becomes, by definition, canonical (N, V, T). The Nose-Hoover model uses the classical temperature concept (discussed in Chapter 6.2.4) based on the instantaneous kinetic energy of the system. The technique of providing thermostatic conditions is of the integral-feedback type. First, an additional term is inserted into Newton's second law of motion

$$\ddot{\mathbf{r}}_i = \frac{\mathbf{F}_i}{m_i} - \vartheta_H \, \xi_H \, \dot{\mathbf{r}}_i \tag{6.19}$$

to control the „jigllings and wigllings" of atoms. Second, the dynamic variable, ξ_H, must satisfy the additional equation of motion

$$\dot{\xi}_H = \vartheta_H \left(\frac{T}{T_0} - 1 \right) \tag{6.20}$$

which provides the necessary feedback. In the differential Equation (6.19), ϑ_H is the coupling speed of the atom with the thermal reservoir. The standard form of Newton's equation of motion is recovered from expression (6.19) for $\vartheta_H = 0$. The variation of the heat distribution variable ξ_H ensures that the long-term average kinetic energy (consequently, the average temperature as well) remains constant, while allowing fluctuations in its current value (Figure 6.10).

Numerical integration of Nose-Hoover equations of motion using the Störmer central difference algorithm ((6.10) and (6.11)) [56] reduces to the following expressions

$$\begin{aligned}
\mathbf{r}(t) &= \mathbf{r}(t-\delta t) + \delta t \, \dot{\mathbf{r}}(t-\delta t/2) + O(\delta t^3), \\
\xi_H(t) &= \xi_H(t-\delta t) + \vartheta_H \left[\frac{T(t-\delta t/2)}{T_0} - 1 \right] \delta t + O(\delta t^3), \\
\dot{\mathbf{r}}\left(t + \frac{\delta t}{2}\right) &= \frac{1}{1 + \vartheta_H \xi_H(t) \delta t/2} \left\{ \dot{\mathbf{r}}\left(t - \frac{\delta t}{2}\right) \left[1 - \frac{1}{2} \delta t \, \vartheta_H \xi_H(t) \right] + \frac{\mathbf{F}(t)}{m} \delta t \right\} + O(\delta t^3).
\end{aligned} \tag{6.21}$$

A detailed consideration of this method is available in [39]. A more advanced version of the thermostat is available in [57].

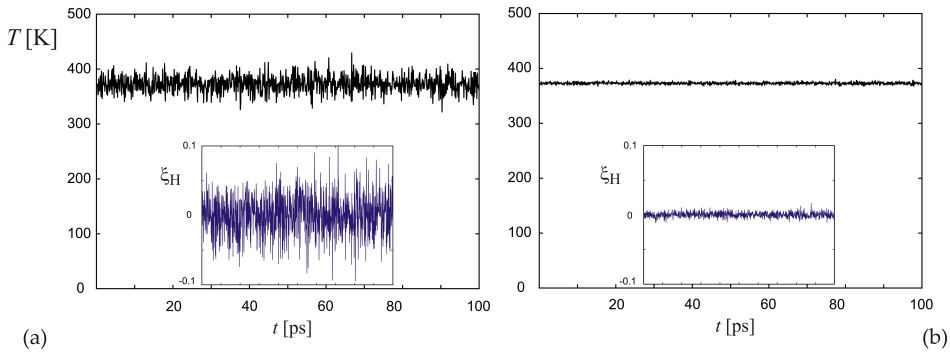

Figure 6.10: Main panels: Examples of current temperature fluctuations in time for a constant mean value of 373[K] in systems with the number of atoms: (a) 1300, and (b) 34000. Inserts: Corresponding fluctuations of the dynamic variable ξ_H which ensure the constant temperature.

6.2.7 Advantages and Disadvantages of Traditional MD

The main advantages of conventional MD methods are:

(i) The only model input (excluding boundary and initial conditions) is the interatomic potential. Other than that, there are no classical constitutive models that postulate the relationships between the main thermomechanical parameters of the state.

(ii) No assumptions are made regarding the nature of the physical mechanisms or simulated processes that are the subject of the study. Accordingly, the possibility opens up for a well-designed virtual experiment to provide a detailed and unbiased insight into the main mechanisms of the studied physical phenomena.

(iii) The above-mentioned insight into the mechanisms of the studied physical phenomena can be achieved with extremely high spatio-temporal resolution.

The main disadvantages of classical MD methods are:

(i) **Classical description of interatomic interactions**, based on empirical potentials, greatly simplifies the rigorous quantum mechanical nature of the material.

(ii) **Classical description of interatomic forces** in which Newton's second law of motion replaces the Schrödinger equation of quantum mechanics. One of the indicators of the validity of this approximation is the de Broglie wavelength, which for thermal motions has the form

$$\Lambda_{th} = \frac{h}{\sqrt{2\pi m k_B T}}$$

where h is the Planck constant, m the atomic mass, k_B is the Boltzmann constant and T is the absolute temperature [16]. Quantum effects are considered to be negligible if the de Broglie wavelength is less than the interatomic distance, $\Lambda_{th} < r_0$, or if the frequency of vibrational motion, ν, is such that $h\nu < k_B T$. In other cases, the atoms of most chemical elements (except the lightest ones like H, He, noble gases) can be considered the material points at sufficiently high temperatures and classical mechanics can be used to describe their motion.

(iii) **Spatio-temporal constraints** which include the size of the MD model and the

duration of the simulated phenomenon, limit the range of problems that can be solved by MD methods.

Although MD has advanced tremendously and gained in popularity on the wave of the extremely rapid development of computer technology, the current state the matter still makes unthinkable the macroscopic modeling of even the shortest physical phenomena. For example, MD modeling of a 1 [mm]^3 copper sample is not even closely achievable, because it consists of approximately 10^{21} copper atoms, which exceeds by far the capabilities of even the most powerful computer systems at present. The size of the MD simulation cell is limited typically up to 10^8 atoms nowadays, which ordinarily corresponds to a few tens of nanometers. According to the available data, it appears that the current record of $4.1 \cdot 10^{12}$ atoms (equivalent to a $4.5 \times 4.5 \times 4.5[\mu m]$ cubic simulation cell) has been achieved on the computer platform "SuperMUC" (Leibniz Supercomputer Center of the Bavarian Academy of Sciences) using 131072 processors and over 500 TFLOPS.

The simulation duration is defined by the size of the time step and the number of cycles. A typical time step in MD simulations is of the order of femtosecond. As an example, for 2D Leonard Jones systems, the initial time step estimate is based on the expression

$$\delta t = \left(\frac{1}{60} \div \frac{1}{30} \right) \frac{2\pi}{\omega_E}, \quad \omega_E = \sqrt{3}\,\omega_0 \tag{6.22}$$

where ω_E denotes the Einstein frequency associated with the fundamental harmonic frequency $\omega_0 = C_0/r_0$ defined in terms of the speed of sound and the equilibrium interatomic distance [39].

The small time step required for MD simulations of atomic systems severely limits the total duration of the event simulated. By using modern computers and massively parallel processing it is possible to calculate approximately 10^8 time cycles (that is, to simulate physical phenomena that occur within 100 [ns]). This is a serious limitation for many problems involving thermally activated processes (Table 6.1, Table 6.2), which is why several methods have been developed for their acceleration for the purpose of studying surface diffusion, film deposition, and the evolution of point defects. A record MD simulation of the order of $10\,[\mu s]$ describes the rapid bending of protein chains [58].

Increasing the physical duration of simulated processes is a constant, active research area that includes the improvement of numerical algorithms, parallel processing, and the continuous development of hardware capabilities.

Table 6.1: Examples of representative temporal and spatial scales necessary to observe some typical deformation mechanisms under step-pressure loading of single-phase metals (adopted from [59]).

Mechanism	Representative Length Scale	Representative Time Scale
Phase transformation	10 nm	10 ps
Dislocation nucleation	50 nm	50 ps
Twin formation	1 nm	1 ns
Interaction of dislocations	100 nm	100 ns
Spallation; tensile damage	1 μm	100 ns
Adiabatic shear	100 μm	10 μs

Table 6.2: Examples of representative temporal and spatial scales necessary to observe some typical deformation mechanisms under step-pressure loading of amorphous brittle materials (adopted from [59]).

Mechanism	Representative Length Scale	Representative Time Scale
Crack nucleation	100 μm	10 ns
Crack coalescence	1 mm	100 ns
Comminution	1 mm	1 μs
Fragment flow	1 mm	1 μs
Interfragment friction	10 mm	10 μs
Interfragment rotation	10 mm	10 μs

(iv) **Output oversaturation** ("data glut"). The above-mentioned detailed insight into the mechanisms of the studied phenomena on the atomic scale with extremely fine time resolution can lead to the oversaturation with the raw MD output data ($\mathbf{r}$,$\mathbf{v}$, $\mathbf{a}$).

6.3 Particle Dynamics

Particle dynamics (PD) is one of many computational methods developed to bridge the gap between the microscopic and macroscopic spatial scales (Figure 6.2). As presented herein, it is an engineering offshoot of MD on an arbitrarily selected spatial scale (Figure 6.11). Since PD has MD techniques at the root, it is sometimes called quasi-MD. Thus, the basic distinguishing features of PD in relation to MD lie in the coarser spatial scale and, in that regard, the phenomenological constitutive model that defines the interparticle interaction. It will be shown in this chapter that this constitutive model may or may not have a functional form of the empirical interatomic potentials. Other than that, the computational simulation techniques used in PD modeling are largely the same as those well known from the traditional MD literature [5], [15], [17]. Greenspan [60] contributed the most to the early development of particle methods as presented in this introduction.

6.3.1 Basic Idea of PD

Basically, the PD system consists of material points (referred to as particles in this chapter) of known masses m_i, and positions $\mathbf{r}_i$ ($i = 1,\ldots,N$). Depending on the material being modeled (fluid, amorphous or crystalline solids), these material points can be arranged randomly or regularly according to the topology of an underlying network. As discussed in Chapter 6.2, the known initial configuration defines the reference state. The calculation methodology requires an approximate solution of the system of differential equations with given initial conditions. At an arbitrary time ($t > 0$), the position and momentum of each particle are completely determined by Newton's laws of motion $(6.1)_1$. Therefore, the movement of each particle is deterministic.

As already mentioned, the well-established MD techniques have been adapted to simulate such coarser-scale material systems with the role of atoms being taken over by a different kind of material points—the large chunks of material—often called a continuum particle or quasi-particle. For simplicity, these material points often interact with each

other according to a simple central-force rule that completely determines the strain energy density function based on their mutual position. A system of Newton differential equations of motion for a system of particles with defined momenta $\mathbf{p}_i = m_i \dot{\mathbf{r}}_i$ is then approximated by an appropriate system of finite difference equations and then solved using one of the many available integration algorithms as outlined in Chapter 6.2.3.

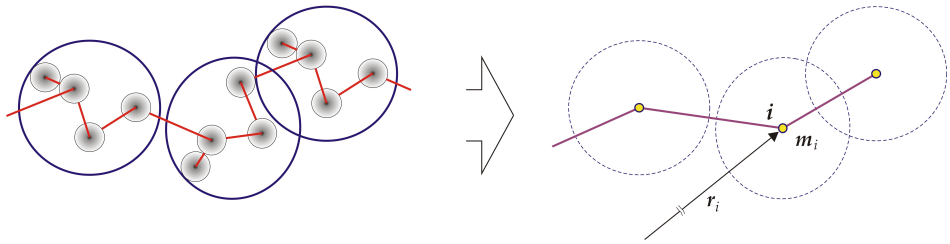

Figure 6.11: Schematic illustration of mapping between a molecular (or atomic) structure and the PD model (represented by a coarse-grained MD model).

It is interesting to note that the time-reversible equation for calculating the next particle position of the system (6.9) can be modified into the following form

$$\mathbf{r}_i(t+\delta t) = \mathbf{r}_i(t) + \eta\,[\mathbf{r}_i(t) - \mathbf{r}_i(t-\delta t)] + \delta t^2\,\mathbf{a}_i(t) \tag{6.23}$$

where η marks the dumping coefficient. The reversible scheme (6.23) is used (often with $\eta = 0.95$) in PD simulations of quasi-static problems for the purpose of dissipating kinetic energy in order to obtain an equilibrium configuration in a time-efficient manner. Assuming that the interparticle forces are conservative, the intensities of the central force with which the particle j acts on the neighboring particle i and the resulting force with which all the first neighbors act on the particle i can be calculated using expression (6.2). The standard form of time-reversible Equation (6.9) is recovered from (6.23) for $\eta = 1$ (no dissiption).

6.3.2 Interparticle Potentials

The interparticle potential (which, as already mentioned, in the PD models plays the role of constitutive law) must be adopted as an initial modeling step. Along with the spatio-temporal scale of simulations, this potential represents the basic difference between MD and PD. One of the most commonly used pair potentials for interparticle interactions

$$\begin{aligned} \phi(r_{ij}) &= -\left(\frac{1}{p-1}\right)\frac{P}{r_{ij}^{p-1}} + \left(\frac{1}{q-1}\right)\frac{Q}{r_{ij}^{q-1}}, \quad q > p > 1, \\ f_{ij} &= -\frac{\mathrm{d}\phi(r_{ij})}{\mathrm{d}r_{ij}} = -\frac{P}{r_{ij}^{p}} + \frac{Q}{r_{ij}^{q}} \end{aligned} \tag{6.24}$$

represents a generalization of the well-known Lennard-Jones 6-12 potential (6.7). The limit case of the exponent $p = 1$ was analyzed in detail by Wang and Ostoja-Starzewski [61] with an alternative form of potential that is necessary due to the singularity of expression

(6.24) for this value of the exponent. With regards to relation (6.24), P, Q, p and q are positive constants, and $q > p$ in order to obtain a repulsive force necessarily much stronger than the attractive one. The Greenspan trailblazing method [60], based on interparticle interaction (6.24), exerted a profound influence on development of PD.

Note that the condition of zero-stress state in the equilibrium configuration $(6.24)_2$ results in the expression for the equilibrium interparticle distance

$$r_{ij0} = \left(\frac{Q}{P}\right)^{\frac{1}{q-p}} \tag{6.25}$$

defined in tems of the four parameters of the interparticle potential $(6.24)_1$. In principle, the equilibrium interparticle distance can be shrinked to the level of a few angstoms in which case the PD model is reduced to the MD model.

An ubiquitous step, common to all CMD methods, is to ensure that the assignment of model parameters results in appropriate physical and mechanical properties of the material. With regards to that crucial step, Wang and Ostoja-Starzewski [61] introduced a novel principle of equivalence between the meso-scale particle model and the micro-scale MD model, while using the Greenspan modeling approach based on the interparticle potential (6.24). This was achieved by establishment of four equality conditions (releted to mass, elastic strain energy, modulus of elasticity and tensile strength) for the purpose of determination of four unknown model parameters in (6.24). In this way, the equations for parameters P, Q, p and q are derived and an appropriate parametric study conducted in order to determine the model parameters under given conditions.

For example, Figure 6.12 shows the dependence of the modulus of elasticity and tensile strength on the parameters (p,q) of the interparticle potential $(6.24)_1$, arrived at by simulations at constant values of the sample volume and the equilibrium interparticle distance [61].

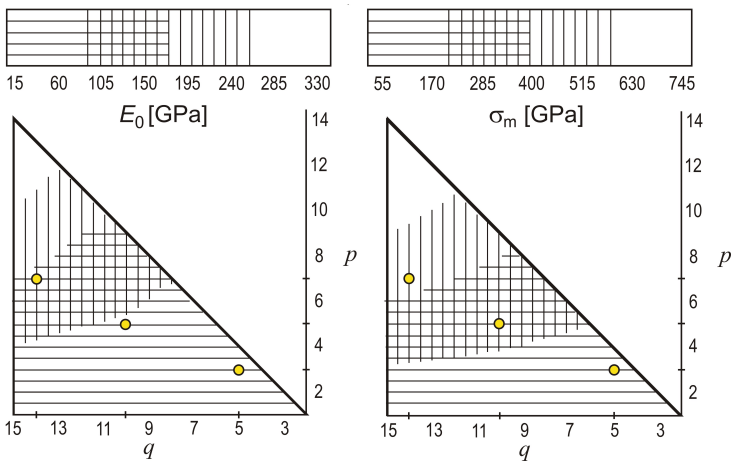

Figure 6.12: Modulus of elasticity and tensile strength dependance upon a pair of parameters (p,q) at fixed values of the interparticle distance (0.2 [cm]) and sample volume $(8.0 \times 11.4 \times 3.1\,[cm^3])$. (Reproduced from reference data [61].)

Given the range of physical characteristics of copper and its alloys ($E_0 = 120 - 150$[GPa] and $\sigma_m = 250 - 1000$[MPa]) it is obvious that, among the three options offered in Table 6.3, the most favorable is $(p,q) = (7,14)$.

It is important to emphasize that this selection is not unique: the similar values of E_0 and σ_m could be obtained with slightly different combinations of parameters (p,q) from which, on the other hand, different values of fracture toughness of materials on the macro-scale can be derived. Accordingly, the analyst has an additional "degree of freedom" to adjust the physical and mechanical properties of the target material to a certain extent.

Another potential that has found wide application in PD [62], for simulations of the behavior of brittle materials with random mesostructure, is a combination of Born-Mayer $(6.26)_1$ and Hookean $(6.26)_2$ potentials.

$$\begin{aligned}
\phi^r(\bar{r}_{ij}) &= \frac{k_{ij} r_{0ij}^2}{(B-2)} \left(\frac{1}{B} e^{B(1-\bar{r}_{ij})} - \bar{r}_{ij}^{-1} \right), \quad \bar{r}_{ij} < 1; \\
\phi^a(\bar{r}_{ij}) &= \frac{1}{2} k_{ij} r_{0ij}^2 (\bar{r}_{ij} - 1)^2, \quad \bar{r}_{ij} \geq 1; \\
f^r(\bar{r}_{ij}) &= \frac{k_{ij} r_{0ij}}{(B-2)} \left(e^{B(1-\bar{r}_{ij})} - \bar{r}_{ij}^{-2} \right), \quad \bar{r}_{ij} < 1; \\
f^a(\bar{r}_{ij}) &= k_{ij} r_{0ij} (\bar{r}_{ij} - 1), \quad \bar{r}_{ij} \geq 1.
\end{aligned} \tag{6.26}$$

In expression for this hybrid potential (6.26), superscripts r and a designate, respectively, a repulsive and attractive branch of interaction, k_{ij} bond stiffness (related to modulus of elasticity by (6.27), while the adjusting parameter B defines the slope (steepness) of the repulsive wall (Figure 6.13, on page 243). The parameter B is, in principle, identifiable from shock experiments (e.g., it is conceptually related to the particle-velocity multiplier in the linear form of the ballistic equation of state) [62].

Table 6.3: Parameters P and Q of potential $(6.24)_1$, modulus of elasticity and tensile strength determined for different pairs of (p,q) parameters shown in Figure 6.12. The reference [61] offers a more precise estimate of these quantities as well as a change in the modulus of elasticity with increasing initial interparticle distance in a given range which is conveyed here in the last line.

(p,q)	(3,5)	(5,10)	(7,14)
P	$2.5 \cdot 10^7$	$1.8 \cdot 10^6$	$1.1 \cdot 10^5$
Q	$9.9 \cdot 10^5$	$5.7 \cdot 10^2$	1.4
$E_0[GPa]$	15.	70.	150.
$\sigma_m[MPa]$	90.	270.	440.
$\Delta E_0[\%]$ $r_0{:}(0.1 \to 0.5)cm$	-15.	-16.	-16.

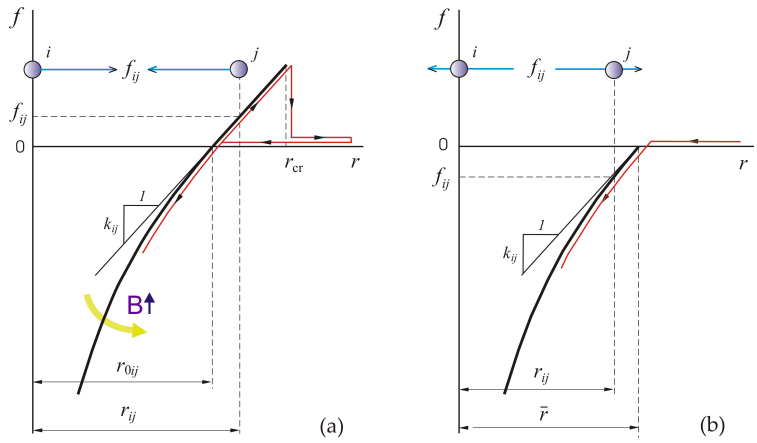

Figure 6.13: Nonlinear hybrid potential (6.26). Schematic representation of the interaction between particles that (a) are or were first-nearest neighbors, and (b) were not first-nearest neighbors initially. The yellow arrow indicates the effect of increasing the parameter B, which defines the slope of the repulsive wall [62].

The latter can be identified in dynamic simulations, for example, by matching the ballistic equation of state. Thus, the average link stiffness of the interparticle potential is determined uniquely by the value of modulus of elasticity of the pristine material

$$k_{ij} = \frac{8}{5\sqrt{3}} E_0^{(3D)}. \tag{6.27}$$

The expression (6.27) is equivalent to (6.41) of the corresponding triangular lattice model with central interactions. This equivalence also implies the fixed value of Poisson's ratio, $\nu^{(3D)} = 1/4$ $(6.39)_1$. The hybrid potential (6.26) was introduced to reproduce some underlying features of the deformation process typical for the considered materials, such as: brittle behavior in tension, increase of shock wave velocity and decrease of compressibility with increasing pressure.

It should be noted that linear interparticle interactions, characteristic of elastic-brittle behavior of materials (and the traditional spring-network models of Chapter 6.4.2), can be considered a modification of the above hybrid potential, with the attractive part of the potential $(6.26)_2$ being used in the repulsion domain as well [63].

Finally, Watson and Steinhauser [64] used a conceptual solution of interparticle interaction very similar to the one of Mastilović and Krajčinović [62] to model the phenomena of hypervelocity impact. The main difference is that their interparticle repulsion instead of the Born-Meyer $(6.26)_1$ used the ubiquitous Lennard-Jones 6-12 potential (6.7), while the Hooke potential $(6.26)_2$ was used in unaltered form in the attractive branch. It is interesting to note that for the purposes of their 3D simulations, Watson and Steinhauser [64] adjusted the remaining two parameters of the model—corresponding to the depth of the potential well in (6.7) and the bond stiffness in $(6.26)_2$ — by a fitting procedure based on a series of hypervelocity impact experiments (a sphere colliding with a thin plate). This nicely illustrates the connection between physical (laboratory) and virtual experiments that is becoming an integral part of contemporary computational modeling.

As already noted, the PD simulation is completely deterministic. However, the particle configurations that mimick the modeled material are not necessarily associated with an ideal lattice. As an example, in order to describe the deformation of the brittle material with a random microstructure, it is necessary to introduce the **quenched disorder** into the computer model. This initial disorder can be topological (unequal coordination number), geometric (unequal bond length) or structural (unequal bond stiffness and/or strength). It can be introduced through the probability distributions of strength, stiffness, and missing bonds (which mimics porosity or pre-existing damage). This (so called, quenched) disorder increases with damage evolution (the induced disorder) in the course of deformation process. Therefore, the nature of damage evolution is inheretly stochastic due to the initial stochasticity of the PD model (although each individual physical realization of the given statistics is deterministic).

6.4 Lattices

Lattice models are a class of CMD models based on the concept of computation domain discretization with an assembly of one-dimensional elements (springs, trusses, beams) endowed by elementary constitutive rules and rupture criteria. They are closely related to PD, as outlined in the preceding chapter, since every system of particles can be associated with a lattice, especially in the case of solids. (As an example, the mentioned modification of the hybrid potential (6.26), with the attractive part of the potential $(6.26)_2$ being used in the repulsion domain as well, constitutes the simplest lattice model - the spring network.) The first application of the lattice method is attributed to the Russo-Canadian engineer Alexander Hrennikoff [7], who devised it to solve the plane stress problem of a thin elastic plate loaded with in-plane forces. The method then fell into oblivion and remained dormant until the 1980s when its remarkable capabilities for introducing material disorder and heterogeneities into the computational model in a simple and natural way were noticed. Ever since, simplicity and inherent ability to capture localized failure mechanisms led to rapid development of lattice models. Not surprisingly, these models are of special importance for studies of mechanical fracture of quasi-brittle materials (e.g., concrete), which were necessarily of phenomenological character. Nonetheless, applications for metals, ceramics, polymers, composites, granular materials are available in literature ([65]-[67]).

The chronological development and adaptations of lattice models to different types of materials and loads are encapsulated herein in a most concise form. To begin with, it should be noted that the continuum can be discretized by lattice models in various ways (plane or spatial lattices, of regular or irregular (random) geometry, with overlapping or non-overlapping elements). Lattice models can also differ in the number of degrees of freedom per node (truss vs. beam), which has proven to be a source of important distinction when it comes to their ability to realistically reproduce physical phenomena. Over time, a consensus was reached that lattice models of irregular geometry with beam interactions were most suitable for fracture simulations, especially in materials characterized with a distinctly heterogeneous structure.

6.4.1 Basic idea of Lattice Models

When formulating the lattice model, it is crucial to establish the relationship between the lattice parameters and the mechanical properties of the solid material being simulated. The gist is that under the uniformly applied load, the lattice should reproduce the linear elastic behavior of the corresponding equivalent continuum and its uniform deformation. Different approaches have been proposed in this regard (e.g., [67]-[71]).

The methodological approach employed herein is based on the **deformation energy** equivalence and follows closely the original works of Ostoja-Starzewski and co-workers [3], [8], [72], [73]. The basic idea is to ensure the equivalence of the deformation energy contained in the deformed unit cell of the lattice (e.g., the hexagonal unit cell in Figure 6.14a) with that in the associated continuum structure (of the same volume V)

$$U_{cell} = U_{continuum}. \tag{6.28}$$

The deformation energy is defined in continuum mechanics by expression

$$U_{continuum} = \frac{1}{2}\int_V \sigma : \varepsilon \, \mathrm{d}V = \frac{1}{2}\int_V \sigma_{\alpha\beta}\varepsilon_{\alpha\beta} \, \mathrm{d}V. \tag{6.29}$$

If we restrict ourselves to a uniform strain field ε, Equation (6.29) becomes

$$U_{continuum} = \frac{V}{2}\varepsilon : \mathbf{C} : \varepsilon = \frac{V}{2} C_{\alpha\beta\gamma\delta}\,\varepsilon_{\alpha\beta}\varepsilon_{\gamma\delta} \tag{6.30}$$

In order to establish relationships between the macroscopic material properties (e.g., the effective stiffness components $C_{\alpha\beta\gamma\delta}$) and the lattice parameters, it is necessary to define a lattice unit cell based on specific periodic arrangements of the associated nodal points and their mutual interactions. For brevity, only the regular triangular lattice with the hexagonal unit cell will be used in the following deliberations (Figures 6.14-6.16).

6.4.2 Lattices with Central Interactions (α Models)

The lattice with central-force interactions (also known as the spring-network or α model) is the basic model in the sense that each bond represents a truss or a spring that transmits only an axial force: $\mathbf{f} = f_n\mathbf{n}$ directed along the bond direction defined by the unit vector $\mathbf{n}$ (Figure 6.14). The deformation energy contained in a unit lattice cell with central interactions is the sum of deformation energies of the constituent lattice elements (bonds)

$$U_{cell} = \sum_b E^{(b)} = \frac{1}{2}\sum_b^{N_b} (\mathbf{f}\cdot\mathbf{u})^{(b)}. \tag{6.31}$$

In Equation (6.31), $\mathbf{u} = \mathbf{u}_{ij} = \mathbf{u}_i - \mathbf{u}_j$ designates the resulting change of length of the lattice element that connects the lattice nodes (material points) i and j, b is bond index (b-th truss/spring), and N_b is their total number. If we restrict ourselves to linearly elastic interactions, Equation (6.31) can be written as

$$U_{cell} = \frac{1}{2}\sum_b^{N_b} (k^n\,\mathbf{u}\cdot\mathbf{u})^{(b)} \tag{6.32}$$

where k^n designated the bond stiffness. (Compare with $(6.8)_1$ and $(6.26)_2$.)

At this point, it is necessary to define an associated unit lattice cell. The derivation of the equations of the connection between the bond (spring) constants and the effective stiffness components is based on equivalence (6.28). A key step in this process is to establish a connection between $\mathbf{u}$ and ε, which depends on the specific geometry of the lattice unit cell and the specific model of the interaction between lattice nodes.

Triangular lattice with central interactions

The only truss lattice to be considered in detail herein is an equilateral triangular lattice with the central-force interactions between the first-nearest neighbors. The lattice, illustrated in Figure 6.14, is based on a hexagonal unit cell and six lattice elements (springs or trusses) of length ℓ, equal to a half the equilibrium distance, r_0, between lattice nodes which defines the equilibrium lattice geometry (the reference state). The area (volume of unit thickness) of a hexagonal unit cell is $V = 2\sqrt{3}\ell^2$. Each bond b, belonging to a given unit cell, is characterized by a spring constant $\alpha^{(b)}$ and unit vector $\mathbf{n}^{(b)}$ defining the bond direction, with corresponding angles $\theta^{(b)} = (b-1)\pi/3$ $(b = 1,\ldots,6)$ with respect to the horizontal.

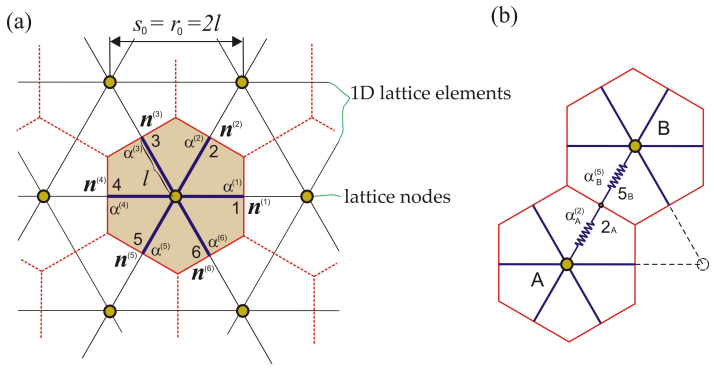

Figure 6.14: (a) Regular triangular lattice with a hexagonal unit cell and central interactions between the first neighbors (α model); (b) a serial connection associated with a link between two adjacent unit cells.

The deformation energy stored in the unit hexagonal cell consisting of six evenly stretched connections is

$$U_{cell} = \frac{1}{2}\sum_{b=1}^{6}(\alpha\,\mathbf{u}\cdot\mathbf{u})^{(b)} = \frac{\ell^2}{2}\sum_{b=1}^{6}\alpha^{(b)}n_\alpha^{(b)}n_\beta^{(b)}n_\gamma^{(b)}n_\delta^{(b)}\,\varepsilon_{\alpha\beta}\varepsilon_{\gamma\delta}. \tag{6.33}$$

Based on equivalence (6.28), the components of the elasticity tensor can be identified in the following form

$$C_{\alpha\beta\gamma\delta} = \frac{1}{2\sqrt{3}}\sum_{b=1}^{6}\alpha^{(b)}n_\alpha^{(b)}n_\beta^{(b)}n_\gamma^{(b)}n_\delta^{(b)} \tag{6.34}$$

which, in the case of equal spring constants $\alpha(b) = \alpha$ $(b = 1, \ldots, 6)$, reduces to

$$\begin{aligned} C_{1111} = C_{2222} &= \frac{9}{8\sqrt{3}}\alpha = \frac{E}{1-\nu^2}, \\ C_{1122} = C_{2211} &= \frac{3}{8\sqrt{3}}\alpha = \frac{E\nu}{1-\nu^2}, \\ C_{1212} = &= \frac{3}{8\sqrt{3}}\alpha = \frac{E}{2(1+\nu)}. \end{aligned} \tag{6.35}$$

It should be noted that expressions (6.35) satisfy the isotropy condition

$$C_{1212} = (C_{1111} - C_{1122})/2. \tag{6.36}$$

In addition, since the value of the apparent plane-strain Poisson's ratio[2] is fixed, the spring constant defines only the plane modulus of elasticity of the unit lattice cell

$$\nu = \frac{C_{1122}}{C_{1111}} = \frac{1}{3}, \quad E = \frac{\alpha}{\sqrt{3}}. \tag{6.37}$$

Importantly, for all types of lattices, the upper limit of the plane Poisson's ratio is defined by the value $(6.37)_1$. This value could be modified in various ways. For example, it is possible to define the so-called "triple honeycomb network" (sometimes the term $\alpha - \beta - \gamma$ model is also used [8]) in which the base of the unit cell is a regular hexagon but, in the notation used in Figure 6.14, $\alpha^{(1)} = \alpha^{(4)} \neq \alpha^{(2)} = \alpha^{(5)} \neq \alpha^{(3)} = \alpha^{(6)}$. This selection of spring stiffnesses results in the following expression

$$\nu = 1 - \frac{2}{\left[1 + \frac{2}{9}\left(\alpha^{(1)} + \alpha^{(2)} + \alpha^{(3)}\right)\left(\frac{1}{\alpha^{(1)}} + \frac{1}{\alpha^{(2)}} + \frac{1}{\alpha^{(3)}}\right)\right]}$$

for the plane Poisson's ratio, which can reproduce values in the range $1/3$ to 1. When $\alpha^{(1)} = \alpha^{(4)} = \alpha^{(2)} = \alpha^{(5)} = \alpha^{(3)} = \alpha^{(6)} = \alpha$, the value $(6.37)_1$ is recovered.

The plane coefficients E and ν, defined by (6.37) in terms of the spring stiffness α, are not material properties but simply their 2D counterparts, mere parameters, obtained by combining the elastic properties under the plane-strain (or, generally, the plane-stress) conditions. Since, the 2D triangular lattice (Figure 6.14) is equivalent to three-dimensional continuum under the plane strain conditions [74], the corresponding relationships between the real (3D) and the **apparent (2D) material properties** are

$$\nu = \frac{\nu^{(3D)}}{1-\nu^{(3D)}}, \quad E = \frac{E^{(3D)}}{1-[\nu^{(3D)}]^2}. \tag{6.38}$$

Consequently, Poisson's ratio and the modulus of elasticity corresponding to Equations (6.37) are

$$\nu^{(3D)} = \frac{1}{4}, \quad E^{(3D)} = \frac{5\sqrt{3}}{16}\alpha. \tag{6.39}$$

[2]The apparent plane-strain Poisson's ratio and the apparent plane-strain modulus od elasticity are henceforth, for brevity, referred to as the plane Poisson's ratio and the plane modulus od elasticity.

Note that the fixed value of Poisson's ratio, $1/4$ $(6.39)_1$, is a reasonable approximation for many engineering materials.

Finally, in lattice modeling it is often useful to designate the spring stiffnesses directly to the bond between two lattice nodes (instead of using the half values associated with the hexagonal unit cell). With regards to Figure 6.14b, since the two springs between the adjacent unit cells A and B are connected in series, their equivalent spring stiffness is

$$\frac{1}{\alpha_{eq}} = \frac{1}{\alpha_A^{(2)}} + \frac{1}{\alpha_B^{(5)}} \quad \Rightarrow \quad \alpha_{eq} = \frac{\alpha_A^{(2)}\,\alpha_B^{(5)}}{\alpha_A^{(2)} + \alpha_B^{(5)}}. \tag{6.40}$$

For the case of equal spring stiffnesses, $\alpha^{(b)} = \alpha$ $(b = 1, \ldots, 6)$, for all unit cells, the preceding expression $(\alpha_{eq} = \alpha/2)$ in combination with $(6.39)_2$ yields

$$\alpha_{eq} = \frac{8}{5\sqrt{3}} E^{(3D)}. \tag{6.41}$$

Thus, Equation (6.41) provides a direct link between the (meso-scale) spring stiffness α_{eq} of the equilateral triangular lattice with the central interactions and the (macro-scale) material property $E^{(3D)}$. (Compare with expression (6.27).)

Chronology of development of lattices with central interactions

Lattices with central interactions, as the simplest lattices, gained popularity very early in the failure modeling of heterogeneous materials with disordered microstructure. Although they began to be used earlier, they achieved the greatest momentum through the pioneering works of Bažant and his associates [67], [68]. Schlangen and van Mier [75], [76] noticed very early the possibilities of the α model to simulate qualitatively the process of damage and fracture of concrete represented by a network of aggregates (as lattice nodes) bonded by the cement (as lattice elements) of inferior tensile strength. However, it should be borne in mind that these simple models are inherently unable to realistically capture more complex crack propagation patterns and reproduce fracture shapes resulting from a combination of basic failure modes [69], [74], [77], [78]. For example, if α models are calibrated to reproduce cracks due to tension and fracture in the first mode, they will do that reasonably well; however, that same model will significantly exaggerate the compressive strength and will not realistically reproduce the stress-strain curve in the post-critical (softening) regime. Also, α models are not able to accurately predict fracture envelopes at complex stress states due to the oversimplified unit-cell stiffness. Despite all of the above, thanks to their simplicity and computational efficiency, these models are—regardless of the abundance of more sophisticated methods—still popular among researchers for simulations in which these shortcomings are not fully expressed [79], [80].

Bažant and co-authors [67], [68], [81] used a central-force lattice with irregular geometry to model the brittle heterogeneous material. In contrast to lattice models in which the distance between nodes is an arbitrary input parameter, they selected the lattice node initial locations by mapping the actual meso-structure of concrete. In other words, the positions of the lattice nodes coincide with the centers of aggregates; therefore, the lattice topology reflects the actual concrete texture. As it will be discussed later, this modeling

approach innovatively introduces the post-critical behavior as a part of the micro-scale constitutive model. Ever since, various approaches were devised to deal with the softening of lattice elements [97]. This model has been immensely influential in development of numerical techniques for these classes of materials (e.g., [70], [82]-[85]).

It cannot be overemphasized that Bažant and co-authors [67], [68] used the **post-critical softening regime** (i.e., the progressive degradation of stiffness) in the constitutive stress-strain relations for the bonding matrix and the interface despite the fact that it is not considered an inherent material property. The softening, thus introduced into the model, is then defined indirectly by the fracture energy of the interparticle bond. More than a decade after this model gained prominence, the assignment of the softening properties to the micro/meso scale has not been not fully defined despite great efforts in that direction (e.g., [86]-[88]). The standard test to determine softening parameters is still elusive due to the unavoidable experimental material-structural interaction. Consequently, the introduction of softening in constitutive relations on the meso-scale was criticized by van Mier [87], on the grounds that there is a danger that the basic mechanisms may be missed due to the fact that the desired results are achieved by introducing additional model parameters. At the same time, many authors advocated the use of softening in constitutive modeling as indispensable (e.g., [89]) since, in their opinion, the meso-scale heterogeneity alone cannot account fully for the experimentally-observed dissipative response at the macro-scale. This difference of opinion is important to point out since the introduction of softening on micro- and meso-scales (based on macroscopic observations) is a common practice as well as an active research topic nowadays due to the computational benefits it provides.

6.4.3 Lattices with Central and Angular Interactions ($\alpha-\beta$ Models)

The lattice with a central-angular interaction (also known as the $\alpha-\beta$ model) was created by upgrading the α model by adding an angular spring between adjacent connections that meet at the same node [90]. Consequently, the energy is necessary to overcome the bending angle resistance reminiscent of $(6.8)_2$.

The triangular $\alpha-\beta$ model was considered in detail by Kale and Ostoja-Starzewski [91] in the context of studying the material damage.

Triangular lattice with central and angular interactions

A triangular lattice with central and angular interactions was obtained by introducing angular springs in the manner illustrated in Figure 6.15. The stiffness of these angular springs is defined by the spring constant $\beta^{(b)}$. According to the conditions of symmetry of the unit cell with respect to the corresponding lattice node, the elastic properties of a hexagonal unit cell are completely determined by six independent spring constants $\{\alpha^{(b)},\beta^{(b)},\ b=1,2,3\}$: $\alpha^{(b)}=\alpha^{(b+3)}$ and $\beta^{(b)}=\beta^{(b+3)}$ for $b=1,2,3$ (isotropic Kirkwood model).

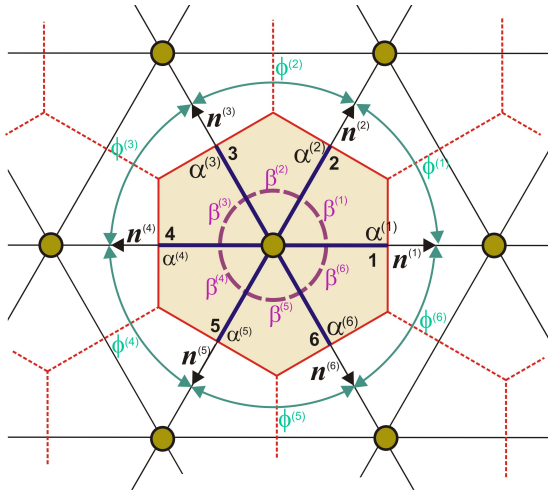

Figure 6.15: A regular triangular lattice with a hexagonal unit cell and a central and angular interaction between the first neighbors ($\alpha-\beta$ model).

The angle of the angular spring with respect to the horizontal axis, in the reference configuration, illustrated in Figure 6.15, is $\theta^{(b)} = (b-1)\pi/3$ $(b = 1,\ldots,6)$. The infinitesimal change of that angle is

$$\Delta\theta^{(b)} = \Delta\theta_{\gamma}^{(b)} = e_{\gamma\alpha\beta}\varepsilon_{\beta\delta}\, n_{\alpha} n_{\delta}, \quad (\alpha,\beta,\delta = 1,2 \text{ and } \gamma = 3) \tag{6.42}$$

with remark that $e_{\gamma\alpha\beta}$ is the permutation tensor (with $\gamma = 3$ for 2D). With regards to Figure 6.15, the corresponding infinitesimal change of the angle between two adjacent bonds (b and $b+1$), associated with the angular spring constant $\beta^{(b)}$, is $\Delta\phi^{(b)} = \Delta\theta^{(b+1)} - \Delta\theta^{(b)}$. Therefore, the deformation energy stored in the angular spring $\beta^{(b)}$ is

$$E_{\beta}^{(b)} = \frac{1}{2}\beta^{(b)}|\Delta\phi^{(b)}|^2 = \frac{1}{2}\beta^{(b)}\left\{e_{\gamma\alpha\beta}\varepsilon_{\beta\delta}\left[n_{\alpha}^{(b+1)} n_{\delta}^{(b+1)} - n_{\alpha}^{(b)} n_{\delta}^{(b)}\right]\right\}. \tag{6.43}$$

The components of the effective stiffness tensor of the triangular $\alpha-\beta$ model can be derived by summation of the deformation energies of the central interactions (6.33) and all six angular springs ((6.43).

Ostoja-Starzewski [3], [8] arrived at the following non-zero components of the effective stiffness tensor

$$\begin{aligned} C_{1111} &= C_{2222} = \frac{1}{2\sqrt{3}}\frac{9}{4}\left(\alpha + \frac{\beta}{\ell^2}\right) = \frac{E}{1-\nu^2} \\ C_{1122} &= C_{2211} = \frac{1}{2\sqrt{3}}\left(\frac{3}{4}\alpha - \frac{9}{4}\frac{\beta}{\ell^2}\right) = \frac{E\nu}{1-\nu^2} \\ C_{1212} &= \frac{1}{2\sqrt{3}}\left(\frac{3}{4}\alpha + \frac{9}{4}\frac{\beta}{\ell^2}\right) = \frac{E}{2(1-\nu)} \end{aligned} \tag{6.44}$$

With respect to Equations (6.44), it can be shown that the isotropy condition (6.36) is satisfied, so that only two independent elastic constants remain. Based on the same

equations, the plane Poisson's ratio and the plane modulus of elasticity can be expressed as functions of the axial (α) and angular (β) spring constants

$$\nu = \frac{C_{1122}}{C_{1111}} = \frac{1}{3}\left[\frac{1-3\beta/(\alpha\ell^2)}{1+\beta/(\alpha\ell^2)}\right], \quad E = \frac{\alpha}{\sqrt{3}}\left[\frac{1+3\beta/(\alpha\ell^2)}{1+\beta/(\alpha\ell^2)}\right] \tag{6.45}$$

Importantly, the two 2D parameters (6.45) are also dependent upon the model resolution defined by ℓ.

Substitution of $\beta = 0$ in Equations (6.45) recovers the plane moduli of the α model defined by Equations (6.37). Complete range of definition of the plane-strain Poisson's ratio

$$-1 < \nu < 1/3$$

can be obtained from expression $(6.45)_1$ for two boundary cases: $\beta/\alpha \to \infty$ and $\beta/\alpha \to 0$ (α model).

The plane moduli of compression and shear are defined as functions of the axial (α) and angular (β) springs constants by the following expressions

$$K = \frac{\sqrt{3}}{4}\alpha, \quad \mu = \frac{\sqrt{3}}{8}\alpha\left(1+3\frac{\beta}{\alpha\ell^2}\right)$$

which demonstrates that angular springs have no effect on volume change.

6.4.4 Lattices with Beam Interactions

The lattice with beam interactions (beam lattice) is the result of upgrading the α model (truss lattice, spring network) by replacing structural elements capable of transmitting only axial force (F) with beam elements that can also transmit shear forces and moments (Q, M; Figure 6.16). The beam lattice represents a **micro-polar continuum** with independent nodal displacement and nodal microrotations fields. As a result there are six (three) degrees of freedom per lattice node in 3D (2D, Figure 6.16c) models. The beam lattice presentation that follows is based mainly on articles of Ostoja-Starzewski [8] and Karihaloo and co-authors [89].

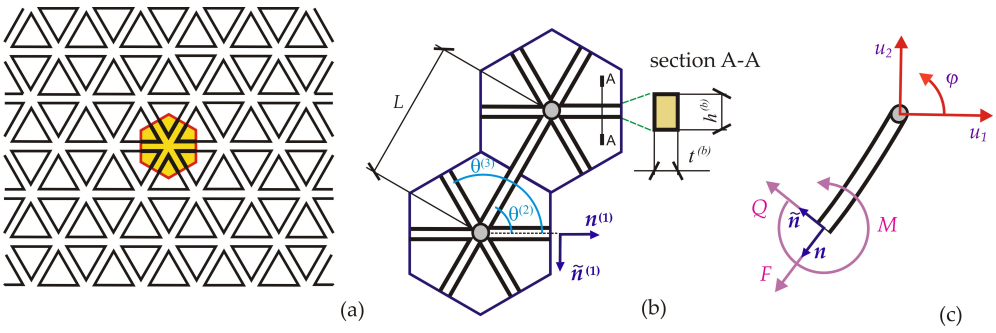

Figure 6.16: (a) Triangular beam lattice with (b) two adjacent hexagonal unit cells; (c) Degrees of freedom per 2D beam lattice node: two translational and one rotational.

Triangular Bernoulli-Euler beam lattice

Bernoulli-Euler beams that transmit axial and shear forces and bending moments are commonly used in beam lattice models to simulate crack propagation and fracture (Figure 6.16). In 2D micropolar continuum ($u_3 = 0$, $\varphi_1 = \varphi_2 = 0$), kinematics of such beam lattice is described with three functions: a nodal displacement (u_1, u_2), and a nodal rotation ($\varphi_3 = \varphi$). The additional kinematic function $\varphi = \varphi_3$ is completely independent of the displacement field (i.e., it is independent and different from the antisymmetric rotation $(u_{j,i} - u_{i,j})/2$ of the classical continuum theory). Adoption of the linearity assumption of the three kinematic functions leads to the expressions for the local asymmetric strain (γ) and the torsional strain (curvature, κ)

$$\gamma_{\alpha\beta} = u_{\beta,\alpha} + e_{\beta\alpha 3}\varphi, \quad \kappa_\delta = \varphi_{,\delta} \tag{6.46}$$

that fully describe the micropolar deformation. With regards to (6.46), recall that $e_{\beta\alpha 3}$ stands for the permutation tensor, and the repeated Greek indices imply summation. Thus, the nodal rotation φ does not contribute to the normal strains (i.e., the elongation of the generic material fiber), which implies that there is no difference between the normal strains in the micropolar and the classical continuum theories ($\gamma_{11} = \varepsilon_{11}$, $\gamma_{22} = \varepsilon_{22}$). The "micro-polar strain" defined by $(6.46)_1$ has the same form as the one used in Cosserat model [92].

The average normal (axial) strain in the half-beam of the unit cell is

$$\gamma^{(b)} = n_\alpha^{(b)} n_\beta^{(b)} \gamma_{\alpha\beta}, \tag{6.47}$$

which is to say that $\gamma^{(b)} L(b)$ is the average change of beam length.

The difference between the angle of rotation of the beam chord and the rotation of its end nodes is

$$\tilde{\gamma}^{(b)} = n_\alpha^{(b)} \tilde{n}_\beta^{(b)} \gamma_{\alpha\beta} = n_\alpha^{(b)} \tilde{n}_\beta^{(b)} u_{\alpha,\beta} - \varphi. \tag{6.48}$$

Where $\mathbf{n}^{(b)}$ and $\tilde{\mathbf{n}}^{(b)}$ designate, respectively, the unit vectors in the longitudinal and lateral directions (Figure 6.16c).

Therefore, the difference between the angles of rotation of the beam ends (corresponding to the lattice nodes) is

$$\kappa^{(b)} \equiv n_\delta^{(b)} \kappa_\delta. \tag{6.49}$$

The Bernoulli-Euler beam theory implies that in each beam the relations between forces and displacements, and moments and angles of rotation, are of the following form

$$F^{(b)} = E^{(b)} A^{(b)} \gamma^{(b)}, \quad Q^{(b)} = \frac{12 E^{(b)} I^{(b)}}{(L^{(b)})^2} \tilde{\gamma}^{(b)}, \quad M^{(b)} = E^{(b)} I^{(b)} \kappa^{(b)}. \tag{6.50}$$

In Equations (6.50) the familiar relations for the area, $A^{(b)} = t^{(b)} \cdot h^{(b)}$, and axial moment of inertia, $I^{(b)} = t^{(b)} [h^{(b)}]^3/12$, of the beam cross-section are used (Figure 6.30b). For the triangular beam lattice with a hexagonal unit cell and the spacing of the mesh $L^{(b)}$ (Figure 6.30), the deformation energy of the unit cell is

$$U_{cell} = \frac{1}{2} \sum_{b=1}^{6} \left[F^{(b)} \gamma^{(b)} + Q^{(b)} \tilde{\gamma}^{(b)} + M^{(b)} \kappa^{(b)} \right] \frac{L^{(b)}}{2}. \tag{6.51}$$

The deformation energy of the equivalent micropolar continuum is

$$U_{continuum} = \frac{1}{2}\left(\gamma_{\alpha\beta} C_{\alpha\beta\gamma\delta} \gamma_{\gamma\delta} + \kappa_\alpha D_{\alpha\beta} \kappa_\beta\right) V \tag{6.52}$$

where $V = (\sqrt{3}/2)L^2 t$ denotes the volume of the continuum corresponding to the unit cell (Figure 6.16b), while t is the thickness (which, in the general case, should be distinguished from the thickness of the half-beam $t^{(b)}$ perpendicular to the lattice plane, shown in Figure 6.16).

The condition of equivalence (6.28) of deformation energies (6.51) and (6.52), leads to the following expressions

$$C_{\alpha\beta\gamma\delta} = \sum_{b=1}^{6} n_\alpha^{(b)} n_\gamma^{(b)} \left[n_\beta^{(b)} n_\delta^{(b)} R^{(b)} + \tilde{n_\beta}^{(b)} \tilde{n_\delta}^{(b)} \tilde{R}^{(b)} \right], \quad D_{\alpha\beta} = \sum_{b=1}^{6} n_\alpha^{(b)} n_\alpha^{(b)} S^{(b)} \tag{6.53}$$

where

$$R^{(b)} = \frac{E^{(b)} A^{(b)}}{\sqrt{3} L t}, \quad \tilde{R}^{(b)} = \frac{12 E^{(b)} I^{(b)}}{\sqrt{3} L^3 t}, \quad S^{(b)} = \frac{E^{(b)} I^{(b)}}{\sqrt{3} L t}. \tag{6.54}$$

It should be noted that, given $(6.54)_1$ and $(6.54)_2$ and the above-mentioned definitions of the cross-sectional properties, it is straightforward to show that

$$\frac{\tilde{R}^{(b)}}{R^{(b)}} = \left(\frac{h^{(b)}}{L^{(b)}}\right)^2 = \left(\bar{h}^{(b)}\right)^2 \tag{6.55}$$

where the height of the beam cross section normalized with its length (Figure 6.16), $\bar{h}^{(b)} = h^{(b)}/L^{(b)}$, represents a geometric parameter inverse of the slenderness of the beam element.

Referring to the properties of the unit cell illustrated in Figure 6.16b

$$\theta^{(b)} = (b-1)\pi/3, \quad \mathbf{n}^{(b)} = \left(n_1^{(b)}, n_2^{(b)}\right) = (\cos\theta^{(b)}, \sin\theta^{(b)}),$$
$$\tilde{\mathbf{n}}^{(b)} = \left(\tilde{n}_1^{(b)}, \tilde{n}_2^{(b)}\right) = (-\sin\theta^{(b)}, \cos\theta^{(b)}), \quad b = 1,2,3,4,5,6$$

and assuming equality of beams $(R^{(b)} = R, \dots)$, the non-zero stiffness components are obtained from (6.53) in the following form

$$\begin{gathered} C_{1111} = C_{2222} = \frac{3}{4} R\left(3 + \frac{\tilde{R}}{R}\right), \quad C_{1122} = C_{2211} = \frac{3}{4} R\left(1 - \frac{\tilde{R}}{R}\right) \\ C_{1221} = C_{2112} = \frac{3}{4} R\left(1 - \frac{\tilde{R}}{R}\right), \quad C_{1212} = \frac{3}{4} R\left(1 + 3\frac{\tilde{R}}{R}\right) \\ C_{2121} = \frac{3}{4} R\left(1 + 3\frac{\tilde{R}}{R}\right), \quad D_1 = D_{22} = 2S. \end{gathered} \tag{6.56}$$

Corresponding Lame coefficients are

$$\mu = \frac{3}{4} R\left(1 + \frac{\tilde{R}}{R}\right) = \frac{\sqrt{3}}{4} \frac{t^{(b)}}{t} \bar{h}(1 + \bar{h}^2) E^{(b)}, \quad \lambda = \frac{3}{4} R\left(1 - \frac{\tilde{R}}{R}\right) = \frac{\sqrt{3}}{4} \frac{t^{(b)}}{t} \bar{h}(1 - \bar{h}^2) E^{(b)} \tag{6.57}$$

and the plane Poisson's coefficient and the modulus of elasticity

$$\nu = \frac{1-\tilde{R}/R}{3+\tilde{R}/R} = \frac{1-\bar{h}^2}{3+\bar{h}^2}, \quad E = 6R\left(\frac{1+\tilde{R}/R}{3+\tilde{R}/R}\right) = 2\sqrt{3}\,\frac{t^{(b)}}{t}\left(\frac{1+\bar{h}^2}{3+\bar{h}^2}\right)E^{(b)} \tag{6.58}$$

based on well-known elasticity relations (e.g., [106]).

Given the expression $(6.58)_1$, it is evident that for slender beams ($h^{(b)} \ll L^{(b)} \Leftrightarrow \bar{h}^{(b)} \ll 1$), shear bending loses importance and the value of the plane Poisson's ratio approaches the upper limit of 1/3. Given the assumption of beam slenderness inherent in the Bernoulli-Euler formulation, the lower limit of the plane Poisson's ratio is ≈ 0.2 [89].

Finally, it is easy to show that in the limit case of negligible shear bending stiffness ($\bar{h} \to 0$), the plane-strain parameters (6.58) are reduced to their α model counterparts (6.37).

The disadvantages of the Bernoulli-Euler beam lattices are: (i) the results are sensitive to the size of the beam elements and the direction of application of the load, (ii) the material response is excessively brittle (especially if ideally-brittle behavior is used for individual beams), (iii) the beam elements in the pressure zones could overlap, and (iv) exceptional computational effort is required at the structural level. All these shortcomings can be reduced in various ways. For example, the first one can be remedied by using an irregular geometry [94]. The second, by 3D modeling, using very small unit cells [95], as well as using a nonlocal approach in calculating the deformations of beam elements [94].

Triangular Timoshenko beam lattice

When the lattice model contains short beams it is more appropriate to use lattice elements based on **Timoshenko beam theory** that takes into account shear deformation and rotational bending effects. This formulation is presented herein in a much abbreviated form in comparison with Bernoulli-Euler beam presented in the preceding chapter. Unlike Bernoulli-Euler formulation, during the actual beam deformation, the cross sections of the beam remain neither perpendicular to the neutral line nor flat/straight (i.e., warping takes place). Timoshenko kept the assumption of a flat section, but introduced an (additional) shear-induced angular deformation, so that the cross section is no longer perpendicular to the neutral line. Thus, Timoshenko beam theory implies

$$Q^{(b)} = \frac{12E^{(b)}I^{(b)}}{(1+\varsigma_T)(L^{(b)})^3}L^{(b)}\tilde{\gamma}^{(b)}, \quad \varsigma_T = \ = \frac{12E^{(b)}I^{(b)}}{G^{(b)}A^{(b)}(L^{(b)})^2} = \frac{E^{(b)}}{G^{(b)}}\bar{h}^{(b)} \tag{6.59}$$

while the relations $F^{(b)} - \gamma^{(b)}$ $(6.50)_1$ and $M^{(b)} - \kappa^{(b)}$ $(6.50)_3$ remain unchanged. The dimensionless parameter $(6.59)_2$ is the key ingredient of Timoshenko beam theory. When the shear stiffness is dominant, $\varsigma_T \ll 1$, the shear displacement is relatively small and Bernoulli-Euler beam theory is applicable. In contrast, at low shear stiffness, the shear displacement is no longer negligible and it is necessary to use Timoshenko beam theory.

From the equivalence of strain energies (6.28), identical expressions for the components of the elasticity tensor (6.56) as for the Bernoulli-Euler beam follow, with the difference that

$$\frac{\tilde{R}}{R} = \frac{12I}{L^2A}\frac{1}{1+\varsigma_T} = \left(\frac{h}{L}\right)^2\frac{1}{1+\varsigma_T} = \frac{\bar{h}^2}{1+\varsigma_T} \tag{6.60}$$

Note that identical geometry of beams is assumed in derivation of Equation (6.60) and the subscript (b) is, consequently, omitted from geometric parameters for brevity. By comparing expressions (6.55) and (6.60), it follows that the stiffness components and elastic constants of Timoshenko beam theory are obtained from Bernoulli-Euler beam theory when $\bar{h}^2$ is replaced by $\bar{h}^2/(1+\varsigma_T)$. Therefore, the plane Poisson's ratio and the modulus of elasticity expressions

$$\nu = \frac{1-\bar{h}^2/(1+\varsigma_T)}{3+\bar{h}^2/(1+\varsigma_T)}, \quad E = 2\sqrt{3}\frac{t^{(b)}}{t}\bar{h}\left(\frac{1+\bar{h}^2/(1+\varsigma_T)}{3+\bar{h}^2/(1+\varsigma_T)}\right)E^{(b)} \tag{6.61}$$

should be used in lieu of (6.58).

In general, Tymoshenko beams are by definition more appropriate for use than Bernoulli-Euler beams when lattice elements are not very slender but rather stocky. As an example, in order to directly include the interface layers in the model (Figure 6.3b), the network resolution (i.e., the beam span) must be limited by the interface thickness. Consequently, there are practical difficulties and extremely large computational efforts. This problem has led to the development of alternative lattice models based on generalized beams [96].

6.4.5 Various Aspects of Lattice Modeling

The selection of lattice elements is crucial for simulation of complex cracking. Schlangen and Garboczi [93], [94] performed a paramount, and later very influential, comparative analysis of simulation techniques using lattice modeling of heterogeneous materials with random micro structure. Experimental crack propagation patterns obtained using a concrete double-edge-notched specimen were compared with those obtained by computer simulations using lattice models with different types of interactions and spatial lattice orientations. The selected results are illustrated in Figure 6.17.

It is important to note that the geometric disorder was not used in these lattice models to emphasize the ability of a particular type of lattice element to capture the fracture pattern. With respect to Figure 6.17, it is obvious that—in the absence of geometric disorder—the beam elements are superior in the reproduction of experimentally observed complex crack patterns compared to the two truss lattices. Nevertheless, it is noticeable that the shape of the cracks even in that case (Figure 6.17d) reveals the bias inevitable in geometrically regular lattices.

Thus, another important selection for correct prediction of complex crack patterns is related to the lattice geometry, especially its regularity. The cracking directions of regular lattices are strongly predetermined (as illustrated in Figure 6.17) but it is easy to achieve the uniform deformation. On the other hand, the irregular lattices are characterized by less biased cracking patterns but, in general, do not behave homogeneously under uniform loading. Schlangen and Garboczi [93] demonstrated importance of the lattice geometric disorder for realistic simulation of crack propagation by comparing crack patterns obtained by computer simulations using four different lattices (based on a square grid, two differently oriented triangular grids, and irregular triangular grids). They also proposed an approach (based on iterative adjustment of the beam properties) to obtain an irregular lattice with the elastically uniform deformation.

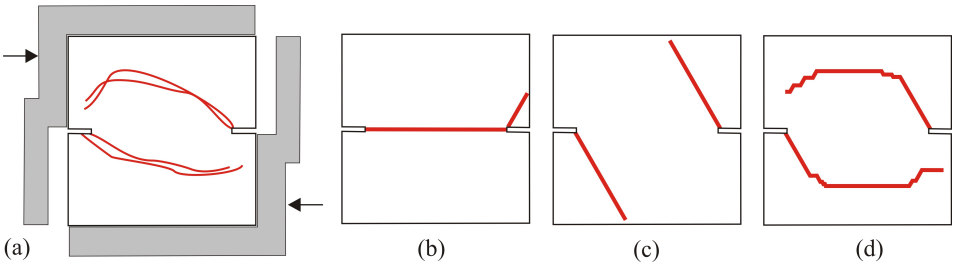

Figure 6.17: Schematic illustration of a prediction of crack path in shear test: (a) the geometries of the experimental setup of the Nuru-Mohammed shear-load test specimen with a double-edge-notched specimen and corresponding crack propagation patterns in a concrete slab (red). Crack propagation patterns were obtained by computational simulations using a **geometrically regular** triangular lattice with: (b) central interaction (Chapter 6.4.2), (c) central-angular interaction (Chapter 6.4.3), and (d) beam interaction (Chapter 6.4.4). (Reproduced based on [93]).

As far as computer implementation procedures are concerned, lattice models simulate the process of damage and fracture by performing an analysis for a given load with the removal from the network of those bonds that meet the prescribed fracture criteria. In the case of beam lattices, the forces and moments are calculated using the appropriate beam theory. A global stiffness matrix is formed for the whole lattice, the corresponding inverse matrix is calculated which is then multiplied by the load vector to obtain the displacement vector. The heterogeneity of the material structure can be taken into account in different ways by: (i) assigning to the beams different tensile strengths, (ii) assuming a random distribution of cross-sectional dimensions and/or beam lengths, or (iii) mapping to beams different material properties (aggregates, cement matrix, interface layers,...; Figure 6.3b). These various types of **disorder** (geometrical, topological, chemical,...) could be introduced by using statistical distributions.

When lattice models are used for fracture analysis, the breaking rule of the basic one-dimensional structural element (that is, the rupture criterion on the micro- or meso-scale) must be defined in advance. Again, depending on the type of material that is the subject of modeling, several bond-removal criteria can be applied based on strength theory, energy dissipation, fracture mechanics. The simplest examples include those used for the lattices with central interactions

$$f^{(b)} = f_{cr}, \quad \varepsilon^{(b)} = \varepsilon_{cr}, \quad \mathrm{E}^{(b)} = \mathrm{E}_{cr}, \tag{6.62}$$

where the critical parameter—as indicated by subscript (cr) — refers to the bond axial force, elongation, or elastic strain energy, respectively.

Naturally, more complex **bond rupture criteria** are commonly used for beam lattices, characterized by more complex stress states. This complexity necessitates the failure definition in terms of the failure envelopes that take into account contributions of all relevant deformation types. For example, van Mier and co-workers [65], [66] established

the following criteria for removal of beam elements

$$\sigma_{eff}^{(b)} = \frac{F^{(b)}}{A^{(b)}} \pm \zeta \frac{(|M_i^{(b)}|, |M_j^{(b)}|)_{max}}{W^{(b)}} = \sigma_{cr}, \qquad \frac{F^{(b)}/A^{(b)}}{\sigma_{cr}} + \frac{|Q^{(b)}|/A^{(b)}}{\sigma_{cr}} > 1 \tag{6.63}$$

where $W^{(b)}$ and ζ designate the section modulus of the beam, and the fitting parameter; while, σ_{cr} and τ_{cr} are the tensile strength and the shear strength, respectively.

With beam lattices, it is possible to reproduce very complex patterns of damage. They are able to simulate the nucleation and propagation of microcracks, crack branching, crack curvature, bridging and coalescence of cracks etc., which results in a complete picture of macroscopic damage and fracture. The model also makes it possible to "capture" the effect of sample size. The advantages of this approach are simplicity and direct insight into the fracture process at the level of the microstructure.

The recent development of lattice models and their "peculiarities" are reviewed recently by Nikolić and co-authors [97].

6.5 Discrete Element Methods

6.5.1 Basic idea of DEM

DEM is a Lagrangian technique of computational simulations in which the computational model is made of discrete (rigid or deformable) elements of the same (or even higher) Euclidean dimensionality as the analyzed problem. These discrete elements of different shapes interact through contact algorithms (smooth or rough contacts) [98]. The material is, therefore, modeled by a set of **Voronoi cells** (mimicking grains, granules, particles, aggregates) representative from the point of view of heterogeneity of material texture, whose meso-scale dynamic interactions determine its macroscopic behavior. Obviously, the contact algorithms are at the physical core of a group of computational techniques custom-made to solve problems characterized by extremely large discontinuities in the internal structure or geometry of materials or both [99]-[101].

DEM was introduced by Cundall [99] to analyze the intermittent progressive fracture of rocky slopes, to be later applied to the analysis of granular assemblies by Cundall and Strack [100]. Although DEM is now widely used for modeling different classes of materials (such as geomaterials, biomaterials, composites), the most natural applications are for simulations of deformation or flow of material systems that have the same topology as the representative group of discrete elements (e.g, Figure 6.1a,c-g). Cundall and Hart [102] summarized succinctly the methodological approach by defining DEM as a method that allows finite translations and rotations of discrete bodies[3] (rigid, solid, breakable), including complete separation of their mutual contacts, as well as automatic recognition of newly established contacts during simulation. The mechanical behavior of the whole

[3]Throughout this chapter, the term "particle" (grain, as well) is used, when convenient, for the DEM building block – the discrete element; it should not be confused with particles used occasionally in relation with other CMD models in this introduction, which are material points.

conglomerate is described on the basis of the motion of these individual elements and specification of the constitutive rules or contact forces among them. Like other methods of CMD, DEM provides a detailed temporal evolution of the system by solving Newton's equations of motion of individual discrete elements (6.1), including the complex damage mechanisms that naturally arise from such simulations. This chapter outlines only the traditional DEM; the review of more advanced DEM models is beyond the scope of this short introduction. The same goes for advanced topics and specifics of DEM technique such as packing and grain shape, flow laws, capillary effects, high deformation loadings, which are available, for example, in the review paper by Donze and co-authors [10] and references cited therein.

It is common to classify DEM models based on the load transfer mechanisms illustrated in Figure 6.18.

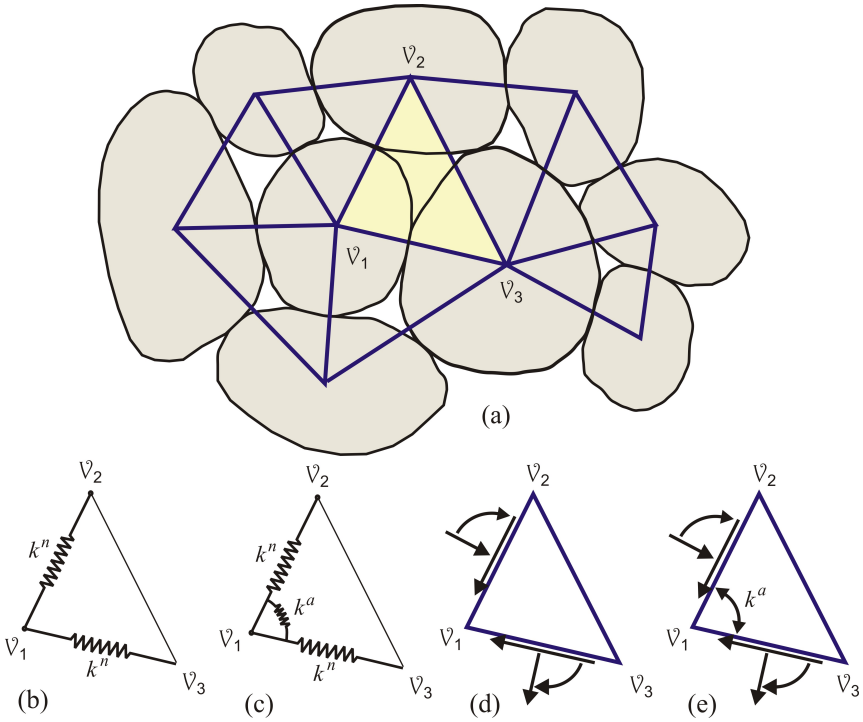

Figure 6.18: (a) A group of particles or grains (with a cluster of three highlighted) with prominent interacting lines forming an associated network. Based on the load transfer mechanism used in the model, DEM are divided into models with: (b) Central interactions (these models represent the generalization of the α model of Chapter 6.4.2); (c) Central and angular interactions (generalization of the $\alpha - \beta$ model of Chapter 6.4.3); (d) Central, shear and bending interactions (generalization of the beam lattices described in Chapter 6.4.4; this is a typical DEM, which can be called a "local inhomogeneous micropolar continuum" [3]); and (e) Central, shear, bending and angular interactions. (Adopted from [3].)

The DEM problem-solving methodology is based on the MD formalism, which includes explicit finite difference schemes in which the computational cycle involves

applying Newton's second law of motion (6.1) to each discrete element using a specified load-displacement rule to all contacts to determine new element positions. During the global conglomerate (sample) evolution, new contacts may appear (between particles that have not previously touched) and existing contacts may disappear. Therefore, the global stiffness matrix of the whole group of discrete elements must be constantly updated, from cycle to cycle. For non-cohesive (loose) materials and particle systems, there is another reason why it is necessary to update the global stiffness matrix: namely, the interactions among discrete elements, both in the normal and shear directions, are not necessarily linear, which means that the stiffnesses k^n and k^t, which define these contacts (e.g., Figure 6.19), must be recalculated continuously [103]-[105].

Unlike computational methods of continuum mechanics, such as FEM, in DEM the role of primary variables is played by forces and displacements. Accordingly, it is necessary to develop and apply methods for describing the continuum parameters (stresses and strains) based on these forces and displacements (i.e., mesoscopic parameters of the state of the individual elements that make up the assembly). This process is called **homogenization**. The starting point in this procedure is to define a **representative volume element**, which serves as an averaging volume for calculating mean values of macroscopic parameters (e.g., [106], [107]). Thus, homogenization and constitutive modeling techniques make it possible to take into account the micro-/meso-structure within the application of continuum methods, but only indirectly in terms of the "mean field". The DEM model parameters are typically adjusted using experimentally observed behavior and a large number of such parameters are necessary to reproduce complex phenomena. The homogenization is, very often, a demanding job because the parameters that control geometric properties and constitutive behavior do not always have a clear physical meaning and can also show complex interdependencies [10]. Despite the open questions highlighted throughout this chapter, DEM modeling (especially the mechanical behavior of geomaterials) is on the rise not only in research but also in geotechnical engineering (e.g., [108]). The main cause of this DEM popularity is the ability of natural reproduction of localization (a phenomenon ubiquitous in quasi-brittle materials with random texture) that is difficult to capture objectively by computational methods of continuum mechanics based on network discretization (e.g., FEM).

6.5.2 Contact Algorithms

It is obvious from the DEM basics outlined above that contact algorithms are the essential DEM feature. Most often, realistic and detailed modeling of particle contacts is not only too complex but also unnecessary. Therefore, in the following considerations, the force of the interaction of the particles i and j is related to their overlap illustrated in Figure 6.19a. The Hertz theory of contact mechanics [109] defines the basic law of elastic contact of two spheres of radius R_i and R_j by a nonlinear relation

$$\left(f_{ij}^n\right)_{ela} = \frac{4}{3}\left(\frac{1-\nu_i^2}{E_i} + \frac{1-\nu_j^2}{E_j}\right)^{-1} \sqrt{R_{ij}}(u_{ij}^n)^{3/2} \tag{6.64}$$

between the normal contact force, f_{ij}^n, and the maximum overlap, u_{ij}. In Equation (6.64), (E,ν) are pairs of elastic constants of two materials in contact and $R_{ij}^{-1} = R_i^{-1} + R_j^{-1}$ the

equivalent radius. The force on particle j exerted by particle i is obtained by applying Newton's third law, $\mathbf{f}^n_{ji} = -\mathbf{f}^n_{ij}$. Equation (6.64) is derived under the following assumptions: (i) the spherical elements are ideally smooth, (ii) the materials are elastic and isotropic, (iii) the shear component of the elastic contact force has no effect on the normal force, and (iv) the overlap is small relative to the size of spherical elements. This law is essential for the simulation of certain phenomena in granular materials, such as the propagation of elastic waves. However, it should be remembered that the **Hertzian contact** model is adequate only for the elastic contact (i.e., when the forces do not exceed the yield strength anywhere in the contact zone). For more complex cases, contact models based on viscoelasticity and elastoplasticity have been developed ([110] and references cited therein).

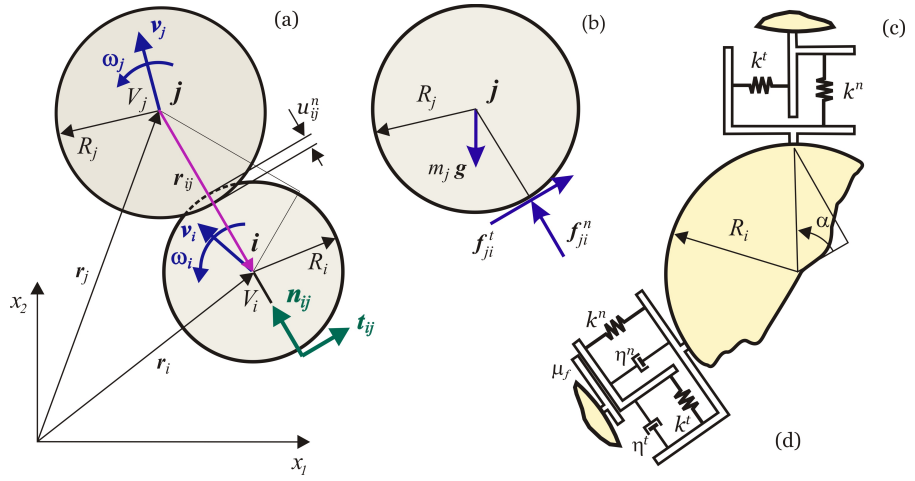

Figure 6.19: Schematic representation of (dry) contact of two circular elements according to the classical theory. (a) Definition of meso-parameters; (b) contact forces; (c) basic interaction model - bonding contact without damping; and (d) a more complex contact model involving damping and friction.

At small deformations, compact geomaterials (e.g., sand in Figure 6.1c) are characterized by a linear elastic response. The force with which two spherical elements of such material act on each other can be decomposed into the elastic normal force, $\mathbf{f}^n_{ela}$, and the incremental shear force, $\mathbf{f}^t$, which are (in the classical interpretation) related to the relative normal and the incremental tangential displacements, respectively, through the coefficients of normal and secant shear stiffness (k^n and k^t)

$$(\mathbf{f}^n_{ij})_{ela} = -k^n \mathbf{u}^n_{ij}, \quad \mathbf{f}^t_{ij} = \{\mathbf{f}^t_{ij}\}_{updated} - k^t \Delta \mathbf{u}^t_{ij}.$$

The elastic response is completely defined by this pair of constants (k^n, k^t). The incremental shear force should reset to zero, $\{\mathbf{f}^t_{ij}\}_{updated} = \mathbf{0}$, whenever the elements can slide relative to each other, which happens when the **Mohr-Coulomb type limit** is reached

$$|f^t_{ij}| = f^t_{coh} + \mu_f f^n_{ij}. \tag{6.65}$$

The limit value (6.65) is defined by the local values of the contact friction coefficient, μ_f, and the cohesion, f^t_{coh} (which is by definition equal to zero for non-cohesive materials).

It cannot be overemphasized that DEM is essentially defined by contact interactions. In addition to the above simple interactions of the discrete elements in contact, more complex contact relationships should be mentioned that take into account subtle details of bonds such as: rotational stiffness (corresponding to rolling stiffness in 2D [66]), capillary cohesion [111], solid cohesion [112], plasticity [113], plasticity with temperature and relaxation [114]. Finally, the general criteria for DEM contact failure are discussed at length by Ibrahimbegovic and Delaplace [115], Tavarez and Plesha [116], Sheng and co-authors [117].

6.5.3 DEM Modeling of Particulate Systems

Particulate systems, as used throughout this DEM overview, include not only non-cohesive (loose) materials but also systems of distinct objects in general (e.g., various industrial transport processes involving flow of "particles" representing a wide variety of objects). The emphasis herein is on the former. Their overall behavior can be described as a contact problem of a large number of bodies, making them ideal for DEM. Therefore, DEM has been used extensively to study the deformation, transport processes, and flow of these **non-cohesive systems** as seen from a number of references such as [66], [118]-[120]. The corresponding numerical techniques are based on the trailblazing work of Cundall and Strack [100]. Since loose materials are large conglomerates of particles, this model, in the absence of adhesion, was based on the "primordial" properties of these discrete elements: their shapes, sizes, and interactions. Discrete elements have two forms of movement, translational and rotational, or three (six) degrees of freedom per element in the case of 2D (3D) problems. Inherently discrete, DEM models represent the non-cohesive system as a group of interacting distinct objects, so computational implementation techniques are based on alternating transitions from the application of Newton's second law of motion (6.1) and the contact force-displacement laws (e.g., Figure 6.19) at every single contact.

Thus, the three main aspects of the particulate system dynamics are:

(i) discrete element shape and size distribution (physical parameters),
(ii) contact behavior of discrete elements (mechanical parameters; e.g., coefficient of contact friction, contact stiffnesses, contact tensile strength), and
(iii) numerical techniques for solving systems of equations of motion (6.1).

The existence or non-existence of the ability of a material to carry tensile loading represents the essential difference between cohesive (adhesive, solid) and non-cohesive (loose, particulate, granular, fluid) materials. The slip aspect of the DEM model takes into account the limited shear resistance—defined by Coulomb's law of friction (6.65) - that the contact provides before sliding.

As particulate systems evolve, collision, sliding, and rolling contacts give rise to forces and moments (Figure 6.19) that the DEM tends to calculate in order to determine new particle positions. The discrete elements - the basic building blocks of the DEM model, can be randomly generalized geometric objects whose size distribution (log-normal is a frequent choice) reflects the inherent heterogeneity of the system. The circular/spherical elements are the simplest option. They are fully described by only one parameter—radius—that defines both their geometry and the one and only type of contact that can be easily observed (Figure 6.19). Accordingly, circles and spheres are often adopted for their simplicity. (For

the same reason - to keep the formalism as simple as possible, the basic equations are presented only for circular geometry in this introduction.) However, this computational convenience comes at a price. First of all, the circular/spherical shape of discrete elements significantly underestimates the rolling resistance among them. Second, they cannot reproduce more complex configurational rearrangements of particles (such as the particle interlock), which typically occur when discrete elements are of more complex shape. These two computational aspects result in an inherent underestimation of macro-strength. An additional artifact introduced by the circular/spherical particle geometry is the numerical porosity, which should not be confused with actual porosity.

Moreover, the discrete elements are often modeled as rigid, but a certain overlap between them (as indicated in Figure 6.19a) is allowed to model the occurrence of relative displacement and localized contact deformation (soft or **smooth contact**). The contact dynamics methods based on "non-smooth" formulations, which exclude the possibility of the particle overlap, are not addressed in this introduction; the interested reader is referred to the review paper of Donze and co-authors [10] and the references cited therein. The rigidity assumption is reasonable when the movements along the interfacial surface represent the largest part of the deformation in the assembly of discrete elements, which is typical for loose materials (such as dry sand Figure 6.1c) and industrial transport processes and flow phenomena. Whatever model is adopted or developed for a certain problem, it will naturally be based on a greater or lesser simplification of the actual physical processes on the meso-scale which is not only inevitable but also desirable, given that many details of the meso-scale contact do not have to be significant for the macro-scale response of the system as a whole. Research challenges include not only realistic quantitative simulations of large particulate systems, with the ability to predict responses and their experimental validation, but also the transition from the meso-scale contact properties to the macroscopic properties of materials. This meso-macro transition should make it possible to understand the collective behavior of the large conglomerate of discrete elements as a function of their contact properties [110].

A typical example of a non-cohesive system are dry granular materials (e.g., dry sands) mentioned above. They are characterized by the dominance of non-cohesive interparticle actions of short range: elastic or inelastic contact forces and contact friction between touching grains. The simplest **rheological model** of such contact interactions is presented in Figure 6.19c with one spring in the normal and tangential directions at the point of contact. According to the more complex approach of Xiang et al. [121], any contact between particles can be rheologically represented by a Kelvin spring-damper element in the normal direction and a spring-damper-slider element in the tangent direction (Figure 6.19d). The contact of the particles in the normal direction is ideally elastic in the case of mutual pressure while the tensile strength of non-cohesive materials is by definition equal to zero. Thus, the generalized contact behavior of particles of a simple central-angular type of interaction (Figures 6.16 and 6.18d represent two isomorphic interaction models) takes into account: normal interactions, shear interactions, and slip. In the general case, the forces acting on the particle j include: the gravitational force $(m_j\mathbf{g})$, and normal $(\mathbf{f}^n_{ji})$ and shear $(\mathbf{f}^t_{ji})$ components of the elastic contact force between elements i and j (Figure 6.19b). Accordingly, taking into account the basic law of dynamics (6.1) and 2D geometry,

the translational and rotational motion of the particle is defined as follows

$$m_i \frac{\mathrm{d}\mathbf{v}_i}{\mathrm{d}t} = m_i \mathbf{g} + \sum_{j=1}^{N_i} \left(\mathbf{f}_{ij}^n + \mathbf{f}_{ij}^t \right), \quad I_i \frac{\mathrm{d}\omega_i}{\mathrm{d}t} = \sum_{j=1}^{N_i} \left(\mathbf{T}_{ij}^t + \mathbf{T}_{ij}^r \right) \tag{6.66}$$

where I_i designates the moment of inertia of particle i, while the translational ($\mathbf{v}$) and rotational (angular) (ω) particle velocities are indicated on Figure 6.19a. $\mathbf{T}_{ij}^t$ is the torque of the tangential component of the contact force, while $\mathbf{T}_{ij}^r$ is the torque of the rolling friction force.

In the case of multiple interactions, the forces and torques on each contact points are evaluated and added to calculate the resultant action on the discrete element. When calculating the contact forces, the contact between the particles is modeled with a pair of linear rheological models of the spring-damper-slider type [100] in both tangential and normal directions (Figure 6.19). Contact force vector $\mathbf{f}_{ij}$, which represents the action of a discrete element j on its neighbor i, can be decomposed into tangential (shear) and normal directions

$$\mathbf{f}_{ij} = \mathbf{f}_{ij}^n + \mathbf{f}_{ij}^t \quad \begin{cases} \mathbf{f}_{ij}^n & = -\left[k^n \mathbf{u}_{ij}^n + \eta^n (\mathbf{v}_{ij} \cdot \mathbf{n}_{ij}) \mathbf{n}_{ij} \right], \\ \mathbf{f}_{ij}^t & = \min\{ k^t \mathbf{u}_{ij}^t - \eta^t \mathbf{v}_{ij}^t, \, \mu_f |\mathbf{f}_{ij}^n| \mathbf{t}_{ij} \} \end{cases} \tag{6.67}$$

wherein both components of the force include dissipative terms, η. The detailed discussion of the this model is presented by Xiang and co-authors [121]. Obviously, Equation (6.67) with $\mu_f = 0$ and $\eta^n = \eta^t = 0$ (no energy dissipation by friction and **damping**) corresponds to the simpler case of Figure 6.19c.

Alonso-Marroquin and Herrmann [122] give an almost identical representation of the DEM methodology, with the discrete elements being in the form of convex polygons. For tetrahedra, one can consult, for example, Munjiza's book [11], and for clusters [123]. Naturally, all grain shapes more complex than circular and spherical ones require much more complex algorithms, for both contact detection and definition of appropriate interactions [122], [124], [125], which will not be subject of this elementary review. However, it should be noted that complex grain shapes are more demanding in terms of computer memory and processing time, which may reduce number of grains that can be used in modeling.

The model parameters (e.g., those figuring in Equation (6.67) and Figure 6.19d) in DEM infancy were typically determined by an ad hoc procedure of calibrating the results of numerical simulations of standard laboratory tests with the corresponding experimental results (e.g., [126]). However, the parameters determined in this way depend on the size of the typical discrete element. Tavarez and Plesha [116] systematically approached the determination of meso-parameters of the model by deriving expressions for elastic stiffness coefficients

$$k^n = \frac{Et}{\sqrt{3}(1-\nu)}, \quad k^t = \frac{1-3\nu}{1+\nu} k^n \tag{6.68}$$

as a function of unit cell thickness t, and the plane elastic coefficients $E = E^{(2D)}$ and $\nu = \nu^{(2D)}$. It should be noted that Equations (6.68) are derived for a densely-packed, ideal triangular 2D lattice using displacement equivalence conditions. The expressions (6.68) also apply to the corresponding irregular lattice obtained by the DEM cluster consolidation process [116]. Also, it should be noted that the condition of non-negativity of

the tangential stiffness coefficient $(6.68)_2$ defines the upper limit for the value of Poisson's ratio $\nu^{(2D)} = 1/3$, which implies $\nu_{\max} = 1/3$ for the plane stress and $\nu_{\max} = 1/4$ the plane strain. Similar expressions for determining the meso-parameters of the DEM model are available in the literature for different spatial arrangements of particles. For example, Masuya et al. [127] and Potyondy and Cundall [128] derived $k^n = Et$, which corresponds to a simple cubic lattice; while Wang and Mora [129] obtained

$$k^n = \frac{E^{(3D)}}{\sqrt{2}(1-2\nu^{(3D)})}, \quad k^t = \frac{1-3\nu^{(3D)}}{1+\nu^{(3D)}} k^n \tag{6.69}$$

for a face-centered cubic lattice.

Equations (6.66) are usually solved by different finite-difference schemes. The Verlet and Störmer algorithms, summarized in Chapter 6.2.3, are often used for this purpose, and the force-displacement law (6.67) and Newton's second law of motion (6.1) are used in each computational cycle. In order to obtain the correct motion of each discrete element by integration, the time step must be chosen carefully as already discussed in Chapter 6.2. By analogy between the contact (with stiffness k^n) and the oscillating material point m, it can be shown that the time step must be chosen as a small part (usually the tenth or twentieth) of the half-period of oscillation [10]. Numerical stability can, for example, be improved by using local, contact dissipative damping as (η^n, η^t) in Equations (6.67).

Finally, the macroscopic constitutive laws of continuum mechanics connect the stress tensor and the specific deformation tensor, while the meso-scale contact constitutive relations connect the contact force with the relative displacement at the points of contact of the particles. Kruyt and Rothenburg [130] derived micromechanical expressions for stress tensors and relative deformations as a function of microscopic contact parameters. The same authors also developed statistical theories of elastic modules for plane groups of particles [131].

6.5.4 DEM Modeling of Solid Materials

The defining property of solid (cohesive) materials is the ability to transfer tensile force between connected particles. Thus, the Cundall's original concept [99], [132], developed for blocky rock systems, has been extended to take into account the interface tensile strength [81], [133], [134]. This DEM adaptation for solid materials was achieved usually by adding a bond at the point of contact of two discrete elements. This bond mimics the presence of a cement matrix attached to the contacting particles, which is able to impart cohesion [135]. This approach has been used to model a wide variety of classes of heterogeneous cohesive materials such as sedimentary rocks, concrete, ceramics, grouted soils, solid rocket propellants, explosives, biomaterials. All these materials, in principle, can be represented by the simple model shown in Chapter 6.5.3 (Figure 6.19) with an important proviso that in the case of cohesive (adhesive) contact, the spring in the normal direction provides resistance to both compressive and tensile loads. If, during the deformation process, the bonded contact between two discrete elements is broken (according to some prescribed bond-rupture criterion), the contact becomes purely compressive and frictional (as illustrated in Figure 6.19), if it survives at all (two grains could be separated instead of pressing against each other). Regarding the simple central and angular interaction (presented in Figure 6.18c and generalized in Chapter 6.4.3) as a combination of a viscoelastic

contact strength model (represented by the Kelvin element) and a slip model, the only difference in non-cohesive and cohesive applications is the ability transmission of the tensile force in the normal direction.

As noted above, DEM models allow the particles of the cohesive material to be interconnected but also separated, if the bond-rupture criterion is met. In the case of the action of an external load such that either the tensile strength or the limit deformation or the fracture energy are exceeded, the bonds between the particles are separated and a crack is formed on the scale of the model (meso, macro). Therefore, damage modes and their interactions naturally arise from the process of gradual particle separation. The DEM approach to discretization of the computational domain is the most pronounced advantage over the continuum-based methods of computational mechanics, since common problems (such as dynamic composite response, crack singularity, crack formulation criterion itself) can be avoided due to naturally discontinuous and random representation of material meso-structure [136].

Application of DEM for rocks

Rock mechanics is the discipline from which DEM originated. The basic idea is to reproduce the quasi-brittle behavior of rocks by simulating the nucleation, growth, branching and merging of local cracks. Although rocks may not look like granular materials at first glance, the main features of many types of rocks and, especially, rock massifs (Figures 6.2h,i) are the pre-existing damage and the high degree of heterogeneity and discontinuity of their structure (at various spatial scales). That is the reason why rock massifs can be considered as conglomerates of discrete blocks interconnected by different models of cohesive forces (“blocky rock systems” [99]). Therefore, the mechanical behavior of the whole jointed-rock assembly evolves from the collective contribution of these discrete blocks during loading. Accordingly, the separation of two discrete units mimics the elementary meso-damage event, which represents the basic building-block of complex damage-evolution phenomena. Detailed reviews by Jing [137] and Jing and Stephansson [98] include techniques, advances, problems, and then predictions of future directions of development in computational rock modeling.

In general, the discrete elements may represent separate rock blocks of (up to) tone and meter levels that, in 2D-DEM rock simulations, can be modeled with randomly generated circles, ellipses, or convex polygons interconnected by introducion of a specific bond into the contact area. The shapes and methods of packing of discrete elements have far-reaching effects on the distribution and intensity of interaction forces. The bond strengths may be allowed to vary from contact to contact, which may represent another source of heterogeneity in the simulated material. The very influential explicit DEM method in rock mechanics is Cundall’s method of "distinct" elements [132], [138] with quadrilateral / prismatic blocks developed in the computer programs UDEC and 3DEC (Itasca^{TM} Consulting Group, www.itascacg.com). The focus of this brief introduction to DEM implementation for rocks will be on a simpler DEM – the **bonded-particle model** (also, often called the parallel-bond model) [128]. This model is based on circular / spherical discrete elements as illustrated in Figure 6.20. This approach to modeling has been generalized by Potyondy [139] and developed over the years through the commercial packages PFC^{2D} and PFC^{3D} (Itasca^{TM} Consulting Group).

Potyondy and Cundall [128] devised the bonded-particle model to simulate rock massifs and other heterogeneous, brittle systems of intermittent sub-structure. In the original variant, the model consisted of a densely packed group of rigid circular/spherical grains of different sizes interconnected at contact points by additional parallel bonds that represent the cohesive action of the cement (Figure 6.20). The rigid discrete elements interact only through soft contacts (i.e., small overlaps are allowed) that possess limited normal and shear stiffness. The model is fully dynamic. It is able to describe complex phenomena of rock damage evolution such as nucleation, growth, branching and merging of microcracks resulting in the damage-induced anisotropy, hysteresis, dilatation, postcritical softening, strength-increasing with lateral confinement. At the beginning of 2000s when this modeling approach commenced, the DEM modeling of discontinuous media was still in its infancy compared to the mechanics of the continuum. Therefore, the authors paid great attention to the systematic development of an appropriate modeling methodology that included not only careful virtual experimentation and qualitative comparison of results with physically observed mechanisms on micro- and macro-scale but also quantitative comparison with experimentally measured properties.

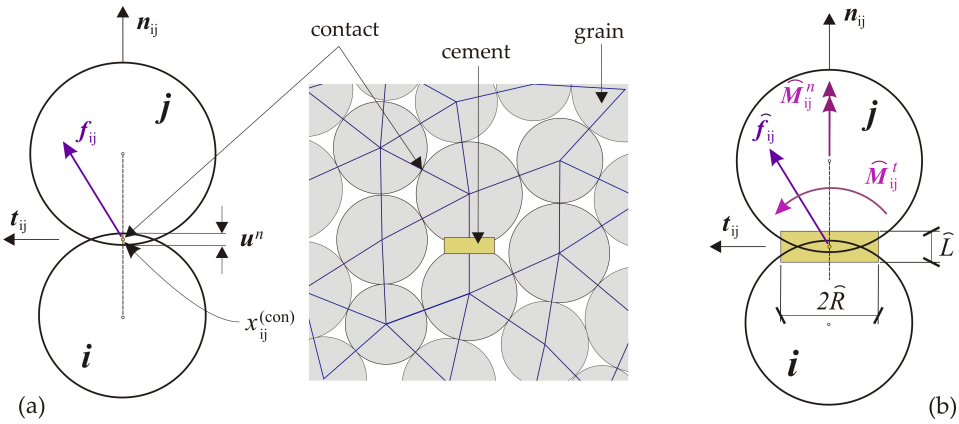

Figure 6.20: Bonded-particle model for simulation of heterogeneous materials composed of cemented grains. Schematics of (a) the behavior of grains in contact (the non-cohesive bond), and (b) cement behavior (the parallel bond). If the cement (which provides the parallel bond) is not present, then only the grain behavior remains and the slip model with rolling (outlined in Chapter 6.5.3) is recovered. In general, the model is defined by the density of the particles, their shape and the size distribution, their packing, and the meso-properties of the grains and the cement. Potyondy and Cundall [128] used circular / spherical elements corresponding to the PFC^{2D} / PFC^{3D} programs (Itasca Consulting Group). Note the striking similarity with the epoxy-cemented glass beads of Figure 6.1a.

It cannot be overemphasized that, unlike some other computational methods in CMD, the term "particle" in this context means a discrete element that occupies a finite part of space (the term “grain” will be also used interchangeably). The radii of the circular discrete elements (particles, grains) are drawn from a uniform distribution bounded by $R_{\min}$ and $R_{\max}$ and dense packaging was obtained by following the appropriate material generation procedure. The rigid particles can independently translate and rotate and interact via soft

contacts (Figure 6.20). They can act on each other exclusively through contacts which are, having in mind their simple shape, always uniquely defined. The grain overlaps are assumed to be small compared to their size to ensure that the contacts occur "at the point". The set of meso-properties consists of the parameters of stiffness and strength of both elements and bonds. The bonds are of finite stiffness and limited strength. The force-displacement dependence in each contact relates the relative displacements of the discrete elements with the forces and moments acting on each of them.

Dynamic response of the system is calculated using a finite difference algorithm comprehensively presented by Cundall and Hart [102]. The DEM simulation technique is based on the assumption that the time step is small enough so that, in one calculation cycle, the perturbations cannot extend beyond the first neighbors of each grain. Potyondy and Cundall [128] discussed in detail the advantages of an explicit numerical scheme. Since DEM is a fully dynamic formulation, attenuation can be introduced as needed to dissipate kinetic energy. This damping mimics microscopic dissipative processes in real materials, such as the internal friction or wave scattering.

Figure 6.20 illustrates the way in which the bonded-particle model simulates the mechanical behavior of a group of circular grains connected by parallel bonds. The total force and moment acting in each contact consist of the contact force $\mathbf{f}_{ij}$, which is the result of the overlap of the particles (Figure 6.20a) and represents the grain behavior (Equation (6.67) with or without damping), and the force and moment, $\hat{\mathbf{f}}_{ij}$ and $\hat{\mathbf{M}}_{ij}$ which are transmitted by the parallel bond and represent the cement behavior (Figure 6.20b). These quantities contribute to the resultant force and moment acting on both circular elements (by virtue of Newton's third law of motion) involved in the contact and represent the input data for computational integration (Newton's second law for a dynamic system (6.1)) using an explicit finite difference scheme to obtain grain trajectories.

The constitutive rule of the contacting grains is described by the same non-cohesive interaction with friction (Chapter 6.5.3 for the case without contact damping) defined with the normal and shear stiffness, k^n and k^t, and the friction coefficient, μ_f. This contact is established as soon as the two grains overlap. The contact stiffnesses of the bond thus established (in the directions normal to, and in, the contact plane, designated respectively by superscripts n and t) are determined by the serial connection (6.40). The overlap, although physically impermissible, mimics, in a sense, the local deformation of the grains (especially when the contact surfaces are not smooth but rough). The contact force vector of each bond can be decomposed into a normal and a shear component as already shown by $(6.67)_1$. The contact behavior of the circular particle is already discussed in Chapter 6.5.3: if $u_{ij}^n \leq 0$ there is a gap (note the sign convention), and the normal and shear forces are equal to zero by definition; if $u_{ij}^n > 0$, there is an overlap, and sliding is defined using the Mohr-Coulomb type limit (6.65). In doing so, in contrast to the normal force (which is at any time proportional to the size of the overlap with secant stiffness, k^n, as the coefficient of proportionality), the shear force is calculated in an incremental manner: after establishing contact, f^t in initialized to zero; from each subsequent increase in the relative displacement of the particles in the direction of the tangent, u^t, there is an increase in shear force, $\Delta f^t = -k^t \Delta u^t$, where k^t tangential stiffness (as opposed to secant from which it is distinguished by the subscript). Contact displacements are calculated in each calculation cycle on the basis of the contact velocity which depends on the translational and angular

velocities of the grains; see the original reference [128] for details.

The behavior of the parallel bond mimicking cement behavior is defined by five parameters: normal and shear stiffness coefficient ($\hat{k}^n, \hat{k}^t$), the tensile and shear strength ($\hat{\sigma}_m, \hat{\tau}_m$), and multiplier $\hat{\lambda}$ which defines the diameter of the parallel bond depending on the diameter of the circular elements in contact. The interaction of the grains is represented by the total force and moment, $\hat{\mathbf{f}}_{ij}$ and $\hat{\mathbf{M}}_{ij}$, transmitted by the parallel bond (Figure 6.20b). The force and moment can be projected in the directions of normal and tangent in the following way

$$\hat{\mathbf{f}}_{ij} = \hat{f}^n_{ij}\mathbf{n}_{ij} + \hat{f}^t_{ij}\mathbf{t}_{ij}, \quad \hat{\mathbf{M}}_{ij} = \hat{M}^n_{ij}\mathbf{n}_{ij} + \hat{M}^t_{ij}\mathbf{t}_{ij} \tag{6.70}$$

where $\hat{f}^n_{ij}$, $\hat{f}^t_{ij}$ denote the normal and shear forces, and $\hat{M}^n_{ij}$, $\hat{M}^t_{ij}$ the twisting and bending (rolling) moments (naturally, there are two of the later in 3D), respectively. (Note that $\hat{M}^n_{ij} \equiv 0$ for 2D models and the bending moment acts in the out-of-plane direction.) At the initialization of the parallel bond, $\hat{f}_{ij}$ and $\hat{M}_{ij}$ are set to zero; each subsequent relative increment of translation and angle of rotation ($\Delta u^n_{ij}, \Delta u^t_{ij}, \Delta\theta_{ij} = (\omega_j - \omega_i)\Delta t$) lead to the corresponding increase in the components of force and moment (Figure 6.20)

$$\Delta\hat{f}^n = \hat{k}^n A \Delta u^n, \quad \Delta\hat{f}^t = -\hat{k}^t A \Delta u^t, \quad \Delta\hat{M}^n = -\hat{k}^t J \Delta\theta^n, \quad \Delta\hat{M}^t = -\hat{k}^n I \Delta\theta^t \tag{6.71}$$

which are added to the current values. The geometrical properties of the parallel-bond cross section in (6.71) — area (A), axial (I) and polar (J) moment of inertia — are defined by well-known expressions in terms of the parallel-bond radius, $\hat{R}$, for the 2D (PFC^{2D}) and 3D (PFC^{3D}) models.

The maximum normal and shear stresses acting on the circumferences of the parallel bond are calculated using the elementary beam theory

$$\hat{\sigma}^{\max} = -\frac{\hat{f}^n}{A} + \frac{|\hat{M}^t|}{I}\hat{R}, \quad \hat{\tau}^{\max} = -\frac{|\hat{f}^t|}{A} + \frac{|\hat{M}^n|}{J}\hat{R} \tag{6.72}$$

If the value of the maximum normal stress $(6.72)_1$ exceeds the tensile strength ($\hat{\sigma}^{\max} \geq \hat{\sigma}_m$) or the maximum shear stress $(6.72)_2$ exceeds shear strength ($\hat{\tau}^{\max} \geq \hat{\tau}_m$), the parallel bond is broken and removed from the model, which corresponds to the nucleation of the tension/shear mesocracks. The cracking of the cement reduces the contact of the corresponding pair of grains (e.g., the glass beads in Figure 6.1a) to the usual non-cohesive interaction with friction.

Potyondy and Cundall [128] demonstrated the ability of this model to reproduce a number of rock behavior characteristics such as fracture, damage-induced anisotropy, dilatation, softening, and confinement-driven strengthening. The evolution of damage is explicitly presented as a process of progressive accumulation of broken ties; "no empirical relations are needed to define damage or to quantify its effect on material behavior " [128]. The obtained damage patterns agree well with the experimental observations and reveal some subtle details of the influence of lateral confinement.

As for the model's ability to reproduce the macroproperties of granite; the modulus of elasticity, Poisson's ratio and uniaxial compressive strength were reproduced with satisfactory accuracy (especially in the case of 3D models). On the other hand, the tensile strength and friction angle obtained by the simulations show large discrepancies with the

experimental results. In particular, there is a marked disparity in strength in the presence of lateral confinement.

Potyondy and Cundall [128] also considered in detail the effect of particle size (given by the minimum diameter of $2R_{min}$ as the defining length scale) on the properties of the material macro-properties. They demonstrated that the discrete-element size is not only an independent parameter of the model that controls the DEM resolution but also an essential part of the material characterization coupled with the macro-properties of tensile strength and fracture toughness. Elastic constants are rather independent of the discrete-element size due to the scaling of the stiffness of the parallel bond as a function of particle size. The unconfined compressive strength seems to show a similar trend of model objectivity. On the other hand, the splitting tensile strength in the Brazilian test ("Brazilian strength") shows a clear dependence on particle size as well as fracture toughness in the first mode (opening). This observation, that the discrete-element size, which controls the model resolution, cannot be chosen arbitrarily because it is coupled with the fracture toughness of the material (expressed by the critical stress intensity factor; K_{Ic}), is not surprising because the very definition of the stress intensity factor implies an internal length scale. Moon and co-authors [140] developed a general procedure for calculating the fracture toughness of random packing of grains of unequal sizes.

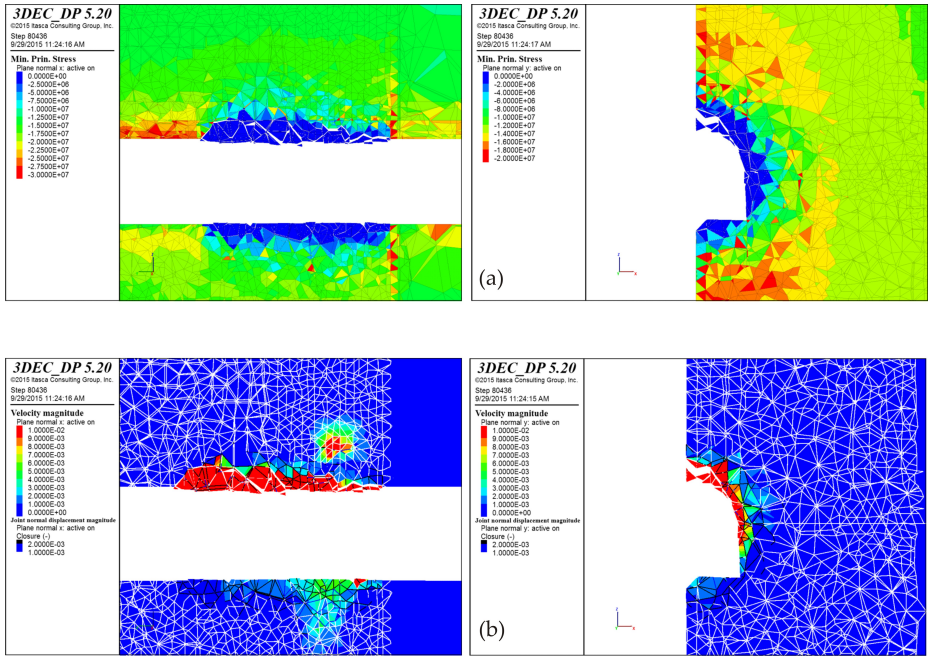

Figure 6.21: 3DEC simulation of collapse of jointed rock masses around an underground excavation due to seismic loading. Field (a) of the maximum principal stress and (b) velocity magnitudes in two planes with given color interpreters. (Courtesy of Dr. Branko Damjanac.)

In line with the observed problems with oversimplified particle shapes, the later model improvements include the use of breakable, deformable, polygonal discrete elements which, in the long run, led to the development of UDEC and 3DEC (Itasca^{TM} Consulting Group) software packages [108]. These programs nowadays represent an indispensable tools for the calculation od intermittent (fractured and jointed) rock massed in the vicinity of underground facilities (Figure 6.21).

Potyondy [141] improved this model by including time-dependent behavior by introducing into the parallel bond the law of damage rate that mimics stress corrosion. Mas Ivars and co-authors [142] performed an important synthesis and rounding up of the whole approach by extending the model of parallel bonds to simulate natural cracks in rock masses by including joints on scales larger than the grain scale. When 3DEC is used to study the stability of cracked rock masses, the considered block is usually divided into several discrete segments defined by the intersection of natural cracks or joints that are piecewise straight (Figure 6.21). These segments (which emulate jointed rock blocks; see Figure 6.1h) are then assigned constitutive properties. The external boundary conditions of discrete segments are set while the internal boundary conditions are calculated from contact interactions which allows explicit modeling of existing cracks in fractured rock [108].

Finally, a detailed overview of the bonded-particle method as a research tool in rock mechanics and engineering applications with current trends and future directions of development is presented by Potyondy [139]. In that reference, an exhaustive list of papers is given in which the method is applied in a wide range of phenomena in rock mechanics and beyond.

Equivalence of beam lattice and DEM representations

A set of nodal points (Figure 6.22a), randomly located in general, can be connected with beams and represented by the beam lattice (Figure 6.22b). Alternatively, these nodal points could be considered centers of circular/spherical particles (Figure 6.22c) connected in the manner illustrated by Figure 6.18d; this particle network is the typical DEM. In general, the stiffness between two particles engaged in contact is represented by the three types of springs (a normal, a shear and a rotational defined, respectively, by the spring constants k^n, k^t, k^a), which is depicted by the symbol shown in Figure 6.22d.

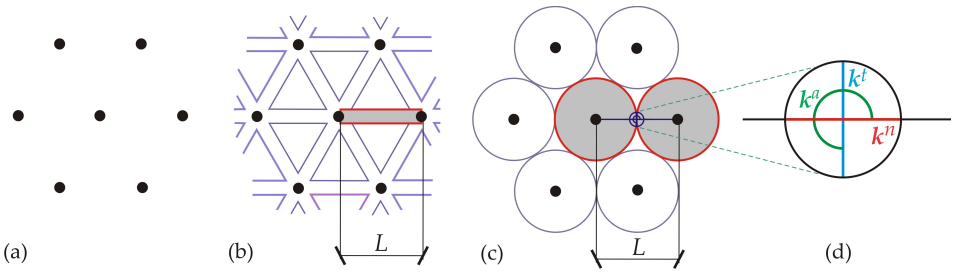

Figure 6.22: (a) A set of nodal points in space and the corresponding: (b) beam lattice and (c) DEM (network of circular particles). (d) The symbol for the particle contact reflecting three types of springs: a normal, a shear, and a rotational.

It is demonstrated by Chang and co-authors [66] that, for a 2D case (the inter-particle twisting stiffness is by definition equal to zero), the behavior of the particle network is equivalent to that of the beam lattice if the following relationships

$$k^n = \frac{E^{(b)}A^{(b)}}{L^{(b)}}, \quad k^t = \frac{12E^{(b)}I^{(b)}}{(L^{(b)})^3}, \quad k^a = \frac{E^{(b)}I^{(b)}}{L^{(b)}}, \tag{6.73}$$

hold true between the spring constants and the beam properties.

Bibliography

[1] Voyiadjis G. (Ed.), 2015, “Handbook of Damage Mechanics: Nano to Macro Scale for Materials and Structures,” Springer Science+Business Media, New York.

[2] D’Addetta, G.A., Kun, F., Ramm, E., Herrmann, H.J., 2001, “From solids to granulates - Discrete element simulations of fracture and fragmentation processes in geomaterials,” P.A.Vermeer et al. (Eds.): LNP 568, pp. 231–258.

[3] Ostoja-Starzewski, M., 2007, “Microstructural randomness and scaling in mechanics of materials.” Taylor & Francis Group, LLC, Boca Raton, FL, USA.

[4] Greenspan, D., 1997, “Particle Modeling,” Birkhäuser Publishing, Boston.

[5] Allen, M.P., Tildesley, D.J., 1987, “Computer Simulation of Liquids,” Oxford University Press Inc., New York.

[6] Wang, G., Cheng, A.H.-D., Ostoja-Starzewski, M., Al-Ostaz, A., Radziszewski, P., 2010, “Hybrid Lattice Particle Modelling Approach for Polymeric Materials Subject to High Strain Rate Loads,” Polymers, 2, 3-30.

[7] Hrennikoff, A., 1941, “Solution of problems of elasticity by the framework method,” J. Appl. Mech., 8, A169–A175.

[8] Ostoja-Starzewski, M., 2002, “Lattice models in micromechanics,” Appl. Mech. Rev., 55(1), 35-60.

[9] Bicanic N., 2004, "Discrete Element Methods;" in Encyclopedia of Computational Mechanics: Fundamentals (eds. Stein et al.), 311-337, DOI: 10.1002/0470091355.ecm006

[10] Donze, F.V., Richefeu, V., Magnier, S-A., 2008, "Advances in Discrete Element Method Applied to Soil, Rock and Concrete Mechanics," Electr. J. Geotech. Engng., Bouquet 08, 1-44.

[11] Munjiza, A., 2004, "The Combined Finite-Discrete Element Method," Wiley, New York.

[12] Alder, B.J., Wainwright, T.E., 1957, "Phase transition for a hardsphere system," J. Chem. Phys., 27, 1208-1209.

[13] Rahman, A., 1964, "Correlations in the Motion of Atoms in Liquid Argon," Phys. Rev., 136, A405.

[14] Levitt, M., Warshel, A., 1975, "Computer simulation of protein folding," Nature, 253, 694.

[15] Haile, J.M., 1992, "Molecular Dynamics Simulations," John Wiley & Sons.

[16] Ercolessi, F.,1997, "A molecular dynamics primer," Spring College in Computational Physics, ICTP, Trieste, Italy.

[17] Rapaport, D.C., 2004, "The Art of Molecular Dynamics Simulations," Cambridge University Press.

[18] Feynman, R.P., 1963, "The Feynman Lectures on Physics," Addison-Wesley.

[19] Born, M., Huang, K., 1956, "Dynamical Theory of Crystal Lattices." Clarendon Press, Oxford.

[20] Stone, A.J., 1996, "The Theory of Intermolecular Forces," Clarendon Press, Oxford.

[21] Lennard-Jones, J.E., Devonshire, A.F., 1939, "Critical and co-operative phenomena," Proc. Royal Soc. A, 169(938), 317-333.

[22] Marenic, E., Soric, J., Ibrahimbegovic, A., 2012, "Adaptive modelling in atomistic-to-continuum mltiscale models," J. Serbian Soc. Comput. Mech., 6(1),169-198.

[23] Ashby, M.F., Jones, D.R.H., 1996, "Engineering Materials 1: An Introduction to Their Properties and Applications," 2nd Edition, Butterworth & Heinemann, Oxford.

[24] Vitek, V., 1996, "Pair potentials in atomistic computer simulations." In: Interatomic potentials for atomistic simulations, MRS Bulletin 21: 20-23.

[25] Daw, M.S., Baskes, M.I., 1984, "Embedded-atom method: Derivation and application to impurities, surfaces, and other defects in metals," Phys. Rev. B, 29, 6443-6462.

[26] Mishin, Y., Farkas, D., Mehl, M.J., Papaconstantopoulos, D.A., 1999, "Interatomic potentials for monoatomic metals from experimental data and ab initio calculations," Phys. Rev. B, 59, 3393-3407.

[27] Holian, B.L., Voter, A.F., Wagner, N.J., Ravelo, R.J., Chen, S.P., Hoover, W.G., Hoover, C.G., Dontje, T.D., 1991, "Effects on pairwise versus many-body forces on high-stress plastic deformation," Phys. Rev. A, 43(6), 2655-2661.

[28] Gullet, P.M., Wagner, G., Slepoy, A., 2004, "Numerical Tools for Atomistic Simulations," SAND2003-8782, Sandia National Laboratories, Albuquerque, NM, USA.

[29] Allen, M.P., 2004, "Introduction to Molecular Dynamics Simulation". In: Computational Soft Matter: From Synthetic Polymers to Proteins, John von Neumann Institute for Computing, Julich, NIC Series, Vol. 23., ISBN 3-00-012641-4, pp. 1-28.

[30] Yip, S. (Ed.), 2005, "Handbook of Materials Modelling," Springer, Berlin.

[31] Plimption, S., 1995, "Fast parallel algorithms for short-range molecular-dynamics," J. Comp. Phys., 117(1), 1-19.

[32] Janežič D., Borštnik U., Praprotnik M., 2009, "Parallel Approaches in Molecular Dynamics Simulations". In: Trobec R., Vajteršic M., Zinterhof P. (eds) Parallel Computing. Springer, London. https://doi.org/10.1007/978-1-84882-409-6-10

[33] Krajcinovic, D., 1996, "Damage Mechanics," Norh-Holland, Amsterdam.

[34] Hoover, W.G., 1985, "Canonical dynamics: Equilibrium phase space distributions," Phys. Rev. A, 31, 1695-1697.

[35] Landau, L.D, Lifshitz, E.M., 1970, "Theory of Elasticity." Pergamon Press, Oxford.

[36] Egami, T., 2011, "Atomic level stress," Progress Mater. Sci., 56, 637–653.

[37] Buehler, M.J., Abraham, F.F., Gao, H., 2003, "Hyperelasticity governs dynamic fracture at a critical length scale," Nature 426: 141-146.

[38] Jou, D., Casas-Vazquez, J., 1992, "Possible experiment to check the reality of a nonequilibrium temperature," Phys. Rev. A, 45, 8371-8373.

[39] Holian, B.L., Voter, A.F., Ravelo, R., 1995. "Thermostatted molecular dynamics: how to avoid the Tada demon hidden in Nose-Hoover dynamics," Phys. Rev. E 52, 2338-2347.

[40] Callen, H.B., 1961, "Thermodynamics," John Willey, New York.

[41] Wannier, G.H., 1987, "Statistical Physics," Dover, New York.

[42] Chandler, D., 1987, "Introduction to Modern Statistical Mechanics," Oxford University Press, New York.

[43] Mastilovic, S., 2016, "Molecular-dynamics simulations of the nanoscale Taylor test under extreme loading conditions," Math. Mech. Solids, 21(3), 326-338.

[44] Fung, Y.C., 1977, "A First Course In Continuum Mechanics," Prentice Hall, Englewood Clifs.

[45] Taylor, G.E., 1948, "The use of flat-ended projectiles for determining dynamic yield stress I. Theoretical considerations", Proc. Royal Soc. London A 194 (1038): 289-299.

[46] Mastilovic, S., 2015, "Impact fragmentation of nanoscale projectiles at ultrahigh striking velocities", Meccanica 50: 2353-2367.

[47] Mesarovic, S.D., Padbidri, J., 2005, "Minimal Kinematic Boundary Conditions for Simulations of Disordered Microstructures," Philosophical Magazine, 85, 65-78.

[48] Parrinello, M., Rahman, A., 1981, "Polymorphic transitions in single crystals: a new molecular dynamics method," J. Appl. Phys., 52, 7182-7190.

[49] Nose, S., Klein, M.L., 1983, "Constant pressure molecular dynamics for molecular systems," Molec. Phys., 50, 1055-1076.

[50] Li, M., Johnson, W.L., 1992, "Fluctuations and thermodynamic response functions in a Lennard-Jones solid," Phys. Rev. B, 46 (9), 5237–5241.

[51] Li, M., Johnson, W.L.,1993, "Ergodicity and convergence of fluctuations in Parrinello-Rahman molecular dynamics," Mat. Res. Soc. Symp. Proc., 291, 285-290.

[52] Verlet, L., 1967, "Computer Experiments on Classical Fluids. I. Thermodynamical Properties on Lennard-Jones Molecules," Phys. Rev., 159(1), 98-103.

[53] Andersen, H.C., 1980, "Molecular dynamics at constrant pressure and temperature," J. Chem. Phys., 72, 2384–2393.

[54] Berendsen, H.J.C. et al, 1984, "Molecular dynamics with coupling to an external bath," J. Chem. Phys., 81(8), 3684–3690.

[55] Nose, S., 1991, "Constant Temperature Molecular Dynamics Methods," Progress Theor. Phys. Supplement, 103, 1-46.

[56] Holian, B.L., De Groot, A.J., Hoover W.G., Hoover C.G., 1990, "Time-reversible equilibrium and nonequilibrium isothermal-isobaric simulations with centered-difference Störmer algorithms," Phys. Rev. A, 41, 4552-4553.

[57] Nose S., 2001, "An improved symplectic integrator for Nose-Poincare thermostat," J. Phys. Soc. Jpn. 70, 75-77.

[58] Freddolino, P.L., Liu, F., Gruebele, M., Schulten, K., 2008, "Ten-microsecond moledular dynamics simulation of a fast folding WW domain," Biophys J. 94(10): L75–L77.

[59] Bourne, N.K., 2011, "Materials' Physics in Extremes: Akrology," Metallurgical Mater Trans A; 42A: 2975-2984.

[60] Greenspan, D., 1997, "Particle Modeling," Birkhäuser.

[61] Wang, G., Ostoja-Starzewski, M., 2005, "Particle modeling of dynamic fragmentation-I: theoretical considerations," Comput. Mater. Sci., 33, 429–442.

[62] Mastilovic, S., Krajcinovic, K, 1999, "High-velocity expansion of a cavity within a brittle material," J. Mech. Phys. Solids, 36, 466-509.

[63] Krajcinovic, D., Vujosevic, M, 1998, "Strain Localization – Short to Long Correlation Length Transition," Int. J. Solids Struct., 35(31-32), 4147-4166.

[64] Watson, E, Steinhauser, M.O., 2017, "Discrete Particle Method for Simulating Hypervelocity Impact Phenomena," Materials, 10, 379; doi:10.3390/ma10040379.

[65] Van Mier, J.G.M., van Vliet, M.R.A., Wang, T.K., 2002, "Fracture mechanisms in particle composites: statistical aspects in lattice type analysis," Mech. Mater., 34, 705–724.

[66] Chang, C.S., Wang, T.K., Sluys, L.J., Van Mier, J.G.M., van Vliet, M.R.A., Wang, T.K., 2002, "Fracture modeling using a micro-structural mechanics approach—I. Theory and formulation," Engrng. Fract. Mech. 69, 1941–1958.

[67] Bažant, Z.P., Tabbara, M.R., Kazemi, M.T., Pyaudier-Cabot, G., 1990, "Random Particle Model for Fracture of Aggregate and Fiber Composites," J. Eng. Mech., 116(8), 1686–1705.

[68] Jirásek, M., Bažant, Z.P., 1995, "Microscopic fracture characteristics of random particle system," Int. J. Fract. 69, 201-228.

[69] Cusatis, G., Bažant, Z.P., Cedolin, L., 2003, "Confinement-shear lattice model for concrete damage in tension and compression, I. Theory," J. Eng. Mech., 129(12), 1439–1448.

[70] Cusatis, G., Bažant, Z.P., Cedolin, L., 2006, "Confinement-shear lattice CSL model for fracture propagation in concrete," Comp. Meth. Appl. Mech. Eng., 195, 7154–7171.

[71] Kozicki, J., Tejchman, J., 2008, "Modelling of fracture process in concrete using a novel lattice model," Granular Matter., 10, 377–388.

[72] Ostoja-Starzewski, M., Wang, G., 2006, "Particle modeling of random crack patterns in epoxy plates," Probabilistic Engng. Mech., 21, 267–275.

[73] Wang, G., Al-Ostaz, A., Cheng, A.H.-D., Mantena, P.R., 2009, "Hybrid lattice particle modeling: Theoretical considerations for a 2D elastic spring network for dynamic fracture simulations," Comput. Mater. Sci. 44, 1126–1134.

[74] Monette, L., Anderson, M.P., 1994, "Elastic and fracture properties of the two-dimensional triangular and square lattices," Modelling Simul. Mater. Sci. Engng., 2, 53-66.

[75] Schlangen, E., van Mier, J.G.M., 1992, "Simple lattice model for numerical simulation of fracture of concrete materials and structures," Mater. Struct., 25, 534–542.

[76] Schlangen, E., van Mier, J.G.M., 1992, “Experimental and numerical analysis of micro-mechanisms of fracture of cement-based composites,” Cem. Concr. Compos., 14, 105–118.

[77] Curtin, W.A., Scher, H., 1990, “Brittle fracture in disordered materials: A spring network model,” J. Mater. Res., 5(3), 535-553.

[78] Jagota, A., Bennison, S.J., 1994, “Spring-Network and Finite Element Models for Elasticity and Fracture.” Proceedings of a workshop on Breakdown and non-linearity in soft condensed matter. K.K. Bardhan, B.K. Chakrabarti, A. Hansen (eds). Springer-Verlag Lecture Notes in Physics (Berlin, Heidelberg, New York) ISBN 3-540-58652-0.

[79] Rinaldi, A., 2009, “A Rational Model for 2D Disordered Lattices Under Uniaxial Loading,” Int. J. Damage Mech., 18, 233-257.

[80] Spagnoli, A., 2009, „A micromechanical lattice model to describe the fracture behavior of engineered cementitious composites,” Comput. Mater. Sci., 46, 7–14.

[81] Zubelewicz, A., Bažant, Z.P., 1987, “Interface element modeling of fracture in aggregate composites,” J. Eng. Mech., 113(11), 1619–1630.

[82] Riera, J.D., Miguel, L.F.F., Iturrioz, I., 2014, “Assessment of Brazilian tensile test by means of the truss-like Discrete Element Method (DEM) with imperfect mesh,” Eng. Struct., 81:10–21.

[83] Rodrigues, R.S., Birck, G., Iturrioz, I., 2016, “Damage index proposals applied to quasi-brittle materials simulated using the lattice discrete element method,” Int. J. Damage Mech., 25 (7), 1017–1039

[84] Đorđevic, N., Vignjevic, R., De Vuyst, T., Gemko, S., Campbell, J., Hughes, K., 2017, “Localization and Damage Induced Softening using Finite Element and Smooth Particle Hydrodynamic Methods,” J. Serbian Soc. Computat. Mech., 11 (2), 120-129.

[85] Iturrioz, I., 2018, “Numerical DEM simulation of the evolution of damage and AE preceding failure of structural components,” Engng. Fract. Mech., https://doi.org/10.1016/j.engfracmech.2018.02.023

[86] Kitsutaka, Y., Uchida, Y., Mihashi, H., Kaneko, Y., Nakamura, S., Kurihara, N., 2001, “Draft on the JCI standard test method for determining tension softening properties of concrete”. In: de Borst et al. (eds). Fracture mechanics of concrete structures, Swets & Zeitlinger, Lisse, 371–376.

[87] Van Mier, J.G.M., 2004, “Lattice modelling of size effect in concrete strength by Ince R, Arslan A, Karihaloo BL [Engineering Fracture Mechanics 2003;70:2307–20],” Eng. Fract. Mech., 71, 1625–1628.

[88] Van Mier, J.G.M., 2007, “Multi-scale interaction potentials (F - r) for describing fracture of brittle disordered materials like cement and concrete,” Int. J. Fract., 143, 41–78.

[89] Karihaloo, B.L., Shao, P.F., Xiao, Q.Z., 2003, “Lattice modelling of the failure of particle composites,” Eng. Fract. Mech., 70, 2385–2406.

[90] Wang, G., Al-Ostaz, A., Cheng, A.H.-D., Mantena, P.R., 2009a, “Hybrid lattice particle modeling: Theoretical considerations for a 2D elastic spring network for dynamic fracture simulations,” Comput. Mater. Sci., 44, 1126–1134.

[91] Kale, S., Ostoja-Starzewski, M., 2015, „Lattice and Particle Modelling of Damage Phenomena;” in Handbook of Damage Mechanics: Nano to Macro Scale for Materials and Structures, Ed. Voyiadjis G., Springer Science+Business Media, New York (DOI 10.1007/978-1-4614-5589-9-23, ISBN 978-1-4614-5588-2), 203-238.

[92] Cosserat, E., Cosserat, F., 1909, “Théorie des corps déformables. Herman, Paris, 1909.

[93] Schlangen, E., Garboczi, E.J., 1996, “New method for simulating fracture using an elastically uniform random geometry lattice,” Int. J. Eng. Science, 34, 1131–1144.

[94] Schlangen, E., Garboczi, E.J., 1997, “Fracture simulations of concrete using lattice models: computational aspects,” Engng. Fract. Mech., 57, 319–332.

[95] Lilliu, G., van Mier, J.G.M., 2003, “3D lattice type fracture model for concrete,” Engng. Fract. Mech., 70, 927–941.

[96] Liu, J.X., Deng, S.C., Zhang, J., Liang, N.G., 2007, “Lattice type of fracture model for concrete”, Theor. Appl. Fract. Mech., 48, 269–284.

[97] Nikolić, M., Karavelić, E., Ibrahimbegovic, A., Miščević P.,2018,"Lattice Element Models and Their Peculiarities," Arch. Computat. Methods Eng., 25, 753–784.

[98] Jing, L.; Stephansson, O., 2008, “Fundamentals of discrete element methods for rock engineering: Theory and applications,” Elsevier, Amsterdam.

[99] Cundall, P.A., 1971, “A computer model for simulating progressive large scale movements in blocky rock systems,” In: Proceedings of the Symposium of International Society of Rock Mechanics, Vol. 1, Nancy: France; 1971. Paper No. II-8.

[100] Cundall, P.A., Strack, O.D.L., 1979, “A discrete numerical model for granular assemblies,” Geotechnique, 29(1), 47–65.

[101] Munjiza, A.A., Knight, E.E., Rougier, E., "Computational Mechanics of Discontiunua," John Wiley & Sons, UK.

[102] Cundall, P.A., Hart, R., 1992, “Numerical modeling of discontinua,” J. Eng. Comp., 9, 101–113.

[103] Van Baars, S., 1996, “Discrete element modelling of granular materials,” Heron.

[104] Li, B., Pandolfi, A., Ravichandran, G., Ortiz, M., 2015, “Material-point erosion simulation of dynamic fragmentation of metals,” Mech. Mater., 80, 288–297.

[105] Kruyt, N.P., Rothenburg, L., 2001, “Statistics of the elastic behavior of granular materials,” Int. J. Solids Struct., 38, 4879-4899.

[106] Nemat-Nasser, S., Hori, M., 1993, "Micromechanics: Overall Properties of Heterogeneous Materials," North-Holland, Amsterdam.

[107] Wellman, C., Lillie, C., Wriggers, P., 2008, "Homogenization of granular material modeled by a three-dimensional discrete element method," Computers and Geotechnics, 35, 394–405.

[108] Damjanac, B., Board, M., Lin, M., Kicker, D., Leem, J., 2007, "Mechanical degradation of emplacement drifts at Yucca Mountain: A modeling case study, part 2: Lithophysal rock," Int. J. Rock Mech. Mining Sci., 44, 368–399.

[109] Maugis, D., 1999, "Contact, adhesion and rupture of elastic solids," Solid-State Sciences, Berlin.

[110] Luding, S., 2008, "Cohesive, frictional powders: contact models for tension," Granular Matter, 10, 235–246.

[111] Yang, S.C., Hsiau, S.S., 2001, "The simulation of powders with liquid bridges in a 2D vibrated bed," Chem. Engng. Sci., 56, 6837–6849.

[112] Delenne, J.-Y., El Youssoufi, M.S., Cherblanc, F., Bénet, J.-C., 2004, "Mechanical behaviour and failure of cohesive granular materials," Int. J. Numer. Analytical Meth. Geomech., 28, 1577–1594.

[113] Shiu, W, Donzé, F.V., Daudeville, L., 2008, "Compaction process in concrete during missile impact: a DEM analysis," Computers and Concrete, 5(4), 329-342.

[114] Luding, S., Manetsberger, K., Muellers, J., 2005, "A discrete model for long time sintering," J. Mech. Phys. Solids, 53(2), 455-491.

[115] Ibrahimbegovic, A., Delaplace, A., 2003, "Microscale and mesoscale discrete models for dynamic fracture of structures built of brittle material," Comput. Struct., 81,1255–1265.

[116] Tavarez, F.A., Plesha, M.E., 2007, "Discrete element method for modelling solid and particulate materials", Int. J. Numer. Meth. Engng., 70, 379–404.

[117] Sheng,Y., Yang, D., TanY, .,Ye, J., 2010, "Microstructure effects on transverse cracking in composite laminae by DEM," Composites Science and Technology, 70, 2093–2101.

[118] Cleary, P.W., Sawley, M.L., 2002, "DEM modeling of industrial granular flows: 3D case studies and the effect of particle shape on hopper discharge," Appl. Math. Model. J., 26, 89-111.

[119] Alonso-Marroquín, F., Muhlhouse, H.B., Herrmann, H.J., 2008, "Micromechanical investigation of soil plasticity using a discrete model of polygonal particles," Theoret. Appl. Mech., 35, 11–28.

[120] Bierwisch, C., Kraft, T., Riedel, X., Moseler, M., 2009, "Three-dimensional discrete element models for the granular statics and dynamics of powders in cavity filling," J. Mech. Phys. Solids, 57(1), 10-31.

[121] Xiang, J., Munjiza, A., Latham,J.-P., Guises, R., 2009, “On the validation of DEM and FEM/DEM models in 2D and 3D,” Engng. Comput., 26(6), 673-687.

[122] Alonso-Marroquín, F., Herrmann, H.J., 2005, “The incremental response of soils. An investigation using a discrete-element model,” J. Engng. Math., 52, 11–34.

[123] Salot, C., Gotteland, P, Villard, P., 2009, “Influence of relative density on granular materials behavior: DEM simulations of triaxial tests,” Granular Matter, 11(4), 221–236.

[124] Kun, F., Herrmann, H.J., 2000, “Damage development under gradual loading of composites,” J. Mater. Sci. 35(18), 4685–4693.

[125] Tykhoniuk, R.,Tomas, J., Luding, S., 2006, “Amicrostructure-based simulation environment on the basis of an interface enhanced particle Model,” Granular Matter 8, 159–174.

[126] Magnier, S.A., Donze, F.V., 1998, “Numerical simulations of impacts using a discrete element method,” Mechanics of Cohesive-Frictional Materials, 3, 257-276.

[127] Masuya, H., Kajukawa, Y., Nakata, Y., 1994, “Application of the distinct element method to the analysis of concrete members under impact,” Nuclear Engnrg. Design, 150 (2-3), 367-377.

[128] Potyondy, D.O., Cundall, P.A., 2004, “A bonded-particle model for rock,” Int. J. Rock Mech. Mining Sci., 41, 1329–1364.

[129] Wang, Y.C., Mora, P., 2008., “Macroscopic elastic properties of regular lattices,” J. Mech. Phys. Solids, 56, 3459–3474.

[130] Kruyt, N.P., Rothenburg, L., 1996, “A micro-mechanical definition of the strain tensor for two dimensional assemblies of particles,” J. Appl. Mech., 63, 706-711.

[131] Kruyt, N.P., Rothenburg, L., 1998, “Statistical theories for the elastic moduli of two-dimensional assemblies of granular materials,” Int. J. Engng. Sci., 36, 1127-1142.

[132] Cundall, P.A., 1980, “UDEC—a generalized distinct element program for modelling jointed rock.” Report PCAR-1-80, Peter Cundall Associates, European Research Office, US Army Corps of Engineers.

[133] Zubelewicz, A., Mroz, Z., 1983, "Numerical simulation of rockburst processes treated as problems of dynamic instability." Rock Mech. Engrg., 16, 253-274.

[134] Plesha, M.E., Aifantis, E.C., 1983, "On the modeling of rocks with microstructure." Proc. 24th U.S. Symp. Rock Mech., Texas A&M Univ., College Station, Texas, 27-39.

[135] Topin, V., Delenne, J.-Y., Radjaï, F., Brendel, L., Mabille, F., 2007, “Strength and failure of cemented granular matter,” Eur. Phys. J. E 23, 413–429.

[136] Yang, D., Sheng, Y., Ye, J., Tan, Y., 2011b, “Dynamic simulation of crack initiation and propagation in cross-ply laminates by DEM,” Composites Sci. Tech., 71, 1410–1418.

[137] Jing, L., 2003, "A review of techniques, advances and outstanding issues in numerical modelling for rock mechanics and rock engineering," Int. J. Rock Mech. Mining Sci., 40, 283–353.

[138] Cundall, P.A., 1988, "Formulation of a three-dimensional distinct element model—Part I: a scheme to detect and represent contacts in a system composed of many polyhedral blocks. Int. J. Rock Mech. Min. Sci. Geomech. Abstr., 25(3),107–116.

[139] Potyondy, D.O., 2014, "The bonded-particle model as a tool for rock mechanics research and application: current trends and future directions," Geosystem Engng., 17 (6), 342–369.

[140] Moon, T., Nakagawa, M., Berger, J., 2007, "Measurement of fracture toughness using the distinct element method," Int. J. Rock Mech. Mining Sci., 44(3), 449-456.

[141] Potyondy, D.O., 2007, "Simulating stress corrosion with a bonded-particle model for rock," Int. J. Rock Mech. Mining Sci., 44, 677–691.

[142] Mas Ivars, D., Pierce, M.E., Darcel, C., Reyes-Montes, J., Potyondy, D.O., Young, R.P., Cundall, P.A., 2011, "The synthetic rock mass approach for jointed rock mass modelling," Int. J. Rock Mech. Mining Sci., 48, 219–244.

Index